Advanced Fiber Materials (2026) 8:262–288
https://doi.org/10.1007/s42765-025-00620-y

RESEARCH ARTICLE

Janus Adhesive Dressing with Macro/Micro Dual Design Enabling Sequential Microenvironment Regulation for Scarless Wound Healing

Meimei Fu[1] · Yue Li[1] · Yitao Zhao[4] · Yuting Zhu[1] · Zhou Fang[1] · Zhuoyi Huang[1,2] · Wenjun Luo[1] · Xinyu Huang[1] · Jintao Li[4] · Zhiqi Hu[1] · Keke Wu[3] · Jinshan Guo[1,2]

Received: 9 April 2025 / Accepted: 1 September 2025 / Published online: 13 November 2025

Abstract

Continuous wound healing micro-environment regulation and timely angiogenesis modulation are crucial for preventing excessive collagen accumulation and promoting scarless wound healing. Herein, a bilayer silk fibroin (SF)-based Janus adhesive dressing (SCE) was developed, featuring a lower layer of Ca^{2+}/Zn^{2+}-modified silk fibroin (SCZ) and an upper layer of silk fibroin core–shell electrospun fibers with epigallocatechin gallate (EGCG) encapsulated in the core (SE). The Ca^{2+}/Zn^{2+} modification induced decrystallization of the SF, thereby conferring strong tissue adhesion to the lower SCZ layer and providing rapid hemostasis and initial anti-inflammatory effects upon wound contact. The macro (double layers) and micro (core–shell) dual design enabled EGCG to be slowly released during the early healing stage, exerting both antioxidant and synergistic anti-inflammatory effects in conjunction with Zn^{2+}. With complete absorption of the lower layer and degradation of the shell of the upper layer, substantial amounts of EGCG were continuously released to inhibit angiogenesis during the later healing stages. In vivo studies employing both rat full-thickness skin wound models and rabbit ear scar models further confirmed the potential of SCE to promote scarless wound healing by combining early-stage hemostatic, antimicrobial, antioxidant, and anti-inflammatory properties with late-stage angiogenesis braking to reduce vascular density and blood supply, thereby allowing extracellular matrix remodeling and preventing collagen overproduction and deposition.

Keywords Janus adhesive · Silk fibroin · EGCG · Antiangiogenesis · Scarless wound healing

1 Introduction

Various forms of fibrosis, including tissue thickening and scarring, are involved in approximately 40% of deaths worldwide [1–3]. In particular, major skin injuries resulting from trauma, burns, or surgery frequently lead to hypertrophic scars (HS) during the healing process, characterized by stiff bulges with reduced tensile strength and impaired pigmentation [4, 5]. These scars can cause itching, chronic pain, and loss of limb mobility and contribute to anxiety and depression, thereby severely affecting the lives of approximately 100 million patients [6–8]. Although numerous studies have explored strategies for the prevention and treatment of scars, which are characterized by excessive dermal fibroblast

Meimei Fu, Yue Li, and Yitao Zhao have contributed equally to this work.

✉ Zhiqi Hu
huzhiqidr163@i.smu.edu.cn

✉ Keke Wu
drwukeke@126.com

✉ Jinshan Guo
jsguo4127@smu.edu.cn

[1] Department of Histology and Embryology, School of Basic Medical Sciences, Department of Plastic and Aesthetic Surgery, Nanfang Hospital of Southern Medical University, Southern Medical University, Guangzhou 510515, People's Republic of China

[2] CAS Key Laboratory of High-Performance Synthetic Rubber and Its Composite Materials, Changchun Institute of Applied Chemistry, Chinese Academy of Sciences, 5625 Renmin Street, Changchun 130022, People's Republic of China

[3] School of Biomedical Engineering, Affiliated Cancer Hospital & Institute, Guangzhou Medical University, Guangzhou 511495, People's Republic of China

[4] Department of Sports Medicine, Center for Orthopedic Surgery, The Third School of Clinical Medicine, Orthopedic Hospital of Guangdong Province, Southern Medical University, The Third Affiliated Hospital of Southern Medical University, Guangzhou 510630, People's Republic of China

proliferation and abnormal extracellular matrix (ECM) deposition during wound healing, HS remains a significant challenge in post-traumatic wound management [4, 9]. While various surgical and nonsurgical approaches, including laser therapy, radiotherapy, cryosurgery, silicone dressings, and topical drug application, have been widely used to treat the existing scars [10, 11], the outcomes remain unsatisfactory due to high recurrence rates and low efficacy [9, 12]. Consequently, early wound healing interventions aimed at preventing scar formation have garnered significant attention and have been proven to be effective approaches for scar treatment [13, 14].

Currently, numerous tissue engineering strategies and bioactive wound matrices have been developed to accelerate wound healing and inhibit scar formation, including strategies based on the targeted management of bacterial infections, elimination of reactive oxygen species (ROS), modulation of the inflammatory microenvironment within the wound, promotion of angiogenesis, regulation of the macrophage phenotype and quantity, and modulation of ECM production [15–20]. Collectively, these methods aim to facilitate wound healing by mitigating adverse factors that hinder rapid wound recovery. Although some strategies for scar prevention targeting specific stages of wound healing have shown partial effectiveness, most of these therapies focus on a single or a few isolated targets of wound healing, failing to sequentially regulate the various stages of wound healing and connect the cascade of biological processes involved in wound healing. Thus, the potential impact of the entire wound healing process on scar formation is frequently neglected [21, 22]. While the intrinsic mechanisms underlying post-traumatic HS formation have not been fully elucidated, the precise coordination of the hemostasis, inflammation, proliferation, and remodeling phases in the early wound healing process is essential to ensure effective wound healing and minimal scar formation [23, 24].

Notably, the regulation of angiogenesis by tissue components is ubiquitous across all four wound healing phases and plays a critical role at each developmental stage [25, 26]. During the hemostasis phase, while angiogenesis has not yet been directly initiated, platelet aggregation and the coagulation cascade triggered by vascular injury cause the release of multiple growth factors (e.g., vascular endothelial growth factor, VEGF, and platelet-derived growth factor, PDGF), which establishes the foundation for subsequent angiogenesis [27]. Upon entering the inflammation phase, cytokines (e.g., VEGF and fibroblast growth factor, FGF) secreted by inflammatory cells such as macrophages pave the way for angiogenesis [28, 29]. In addition, the local hypoxic environment, through the activation of hypoxia-inducible factor 1 alpha (HIF-1α), further stimulates the expression of pro-angiogenic factors such as VEGF, providing a critical signal for angiogenesis in the proliferation phase [30]. During the proliferation phase, neovascularization represents a critical biological process. These neovessels deliver adequate oxygen and nutrient supplies to fibroblasts, epithelial cells, and immune cells, thus supporting cellular proliferation and migration processes [31]. Simultaneously, these neovessels deliver key growth factors (e.g., epidermal growth factor, EGF, and transforming growth factor-β, TGF-β) that facilitate granulation tissue generation, collagen synthesis, epithelialization, and the restoration of cellular metabolism and functionality [32, 33]. During the remodeling phase, tissues undergo optimization of vascular density and functionality through neovasculature maturation and the degradation of redundant blood vessels, thus establishing the foundation for the organized arrangement of collagen fibers and the functional remodeling of tissues [34, 35]. Therefore, precisely regulated angiogenesis and epithelialization constitute the essential prerequisites for proper collagen deposition and organization within the wound matrix [36]. Traditionally, early angiogenesis generally exerts beneficial effects in wound healing, whereas reduced or inhibited angiogenesis negatively impacts the healing process [37]. However, emerging evidence has demonstrated that excessive vascularization is not always beneficial, especially during the proliferation and remodeling phases of the wounds [38, 39]. Sustained overexpression of angiogenesis-related signaling molecules during late healing stage frequently leads to HS or keloid formation [5]. Notably, studies have confirmed that scar tissue exhibits a highly vascularized structural composition [40], suggesting that the stage-specific regulation of angiogenesis represents a crucial strategy for optimizing wound healing outcomes [41, 42]. Therefore, an innovative material design strategy that facilitates wound repair through sustained modulation of the healing microenvironment to eliminate deleterious factors, while dynamically regulating inflammation, neovascularization, collagen deposition, and matrix remodeling, may represent an optimal approach for achieving scarless wound healing [34].

To achieve sustainable modulation of the wound healing microenvironment and phased pro- and anti-angiogenesis, silk fibroin (SF), a well-recognized biocompatible natural polymer with minimal inflammatory response [43, 44], was chosen to develop a bilayer Janus adhesive dressing (SCE) composed of a Ca^{2+}/Zn^{2+}-modified SF lower layer and a SF-based core–shell electrospun fiber upper layer (Scheme 1). Meanwhile, to control the disordered growth of neovasculature, EGCG, a plant polyphenol with anti-inflammatory and anti-angiogenic properties [45, 46], was encapsulated within the core of the upper layer through coaxial electrospinning with SF. The SCE Janus adhesive dressings provided effective exudate management capabilities through its unique Janus structure. The Ca^{2+}/Zn^{2+} modification not only induced silk fibroin decrystallization, endowing the lower layer with strong tissue adhesiveness, but also imparted rapid hemostatic capability and anti-inflammatory properties. The macro (double layers) and micro (core–shell) dual design enabled the slow release of EGCG during the early

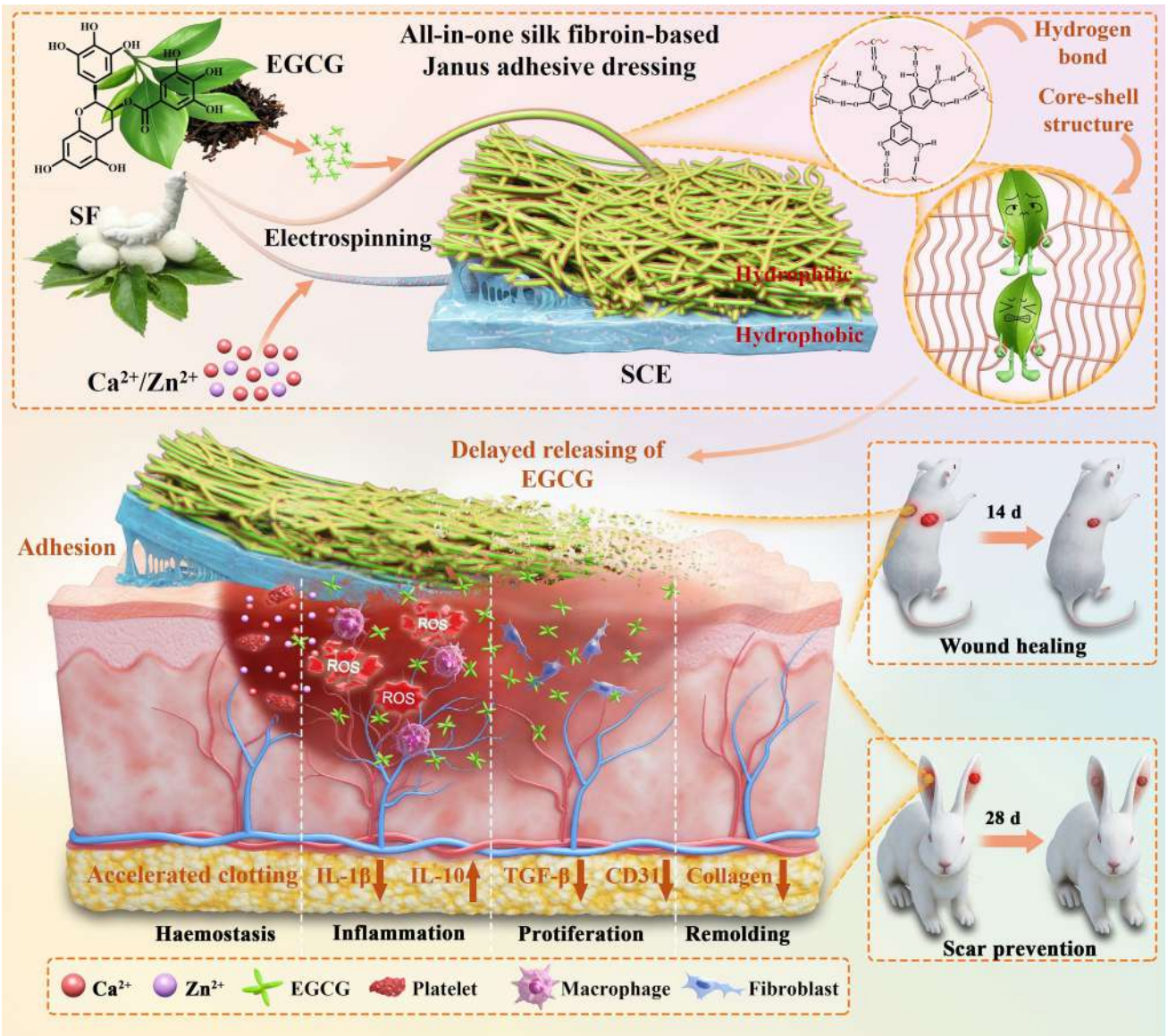

Scheme 1 Development of a Janus adhesive dressing with macro/micro dual design enabling sequential microenvironment regulation for scarless wound healing

stage of wound healing, exerting antioxidant ability and anti-inflammatory activity synergistic with Zn^{2+}. Following rapid and complete absorption of the lower layer, the core–shell electrospun fiber layer directly contacted with the wound. Possessing a high surface area-to-volume ratio and favorable cell adhesiveness [11], the upper layer can not only promote fibroblast migration and granulation tissue formation, but also accelerate epithelialization, thereby significantly promoting wound healing. Subsequently, along with the degradation of the shell of the core–shell electrospun fibers, a substantial amount of anti-angiogenetic EGCG was continuously released from the core of the core–shell electrospun fibers, effectively regulating neovascularization during the proliferation and remodeling phases of wound healing. This process effectively inhibited excessive angiogenesis and collagen deposition while regulating ECM degradation and remodeling, ultimately achieving scarless wound healing. In vivo studies utilizing both rat full-thickness skin wound and rabbit ear scar models further validated the scarless wound healing efficacy of SCE.

2 Results and Discussion

2.1 Fabrication and Characterizations of Silk Fibroin-Based Janus Adhesive Dressings

A series of silk fibroin-based adhesive dressings with different lower and upper layers were developed via

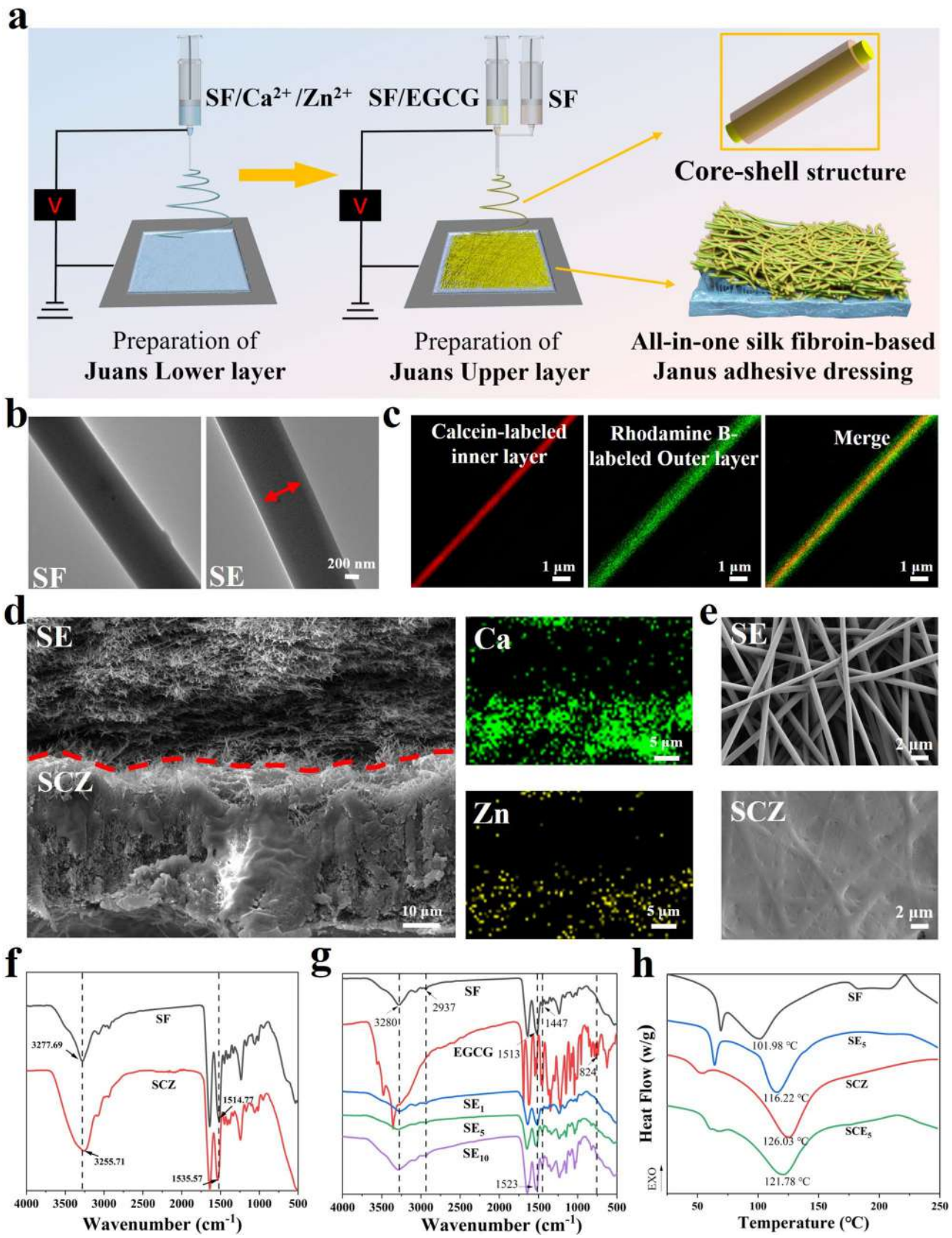
a
SF/Ca2+ /Zn2+
SF/EGCG
SF
V
V
Core-shell structure
Preparation of
Juans Lower layer
Preparation of
Juans Upper layer
All-in-one silk fibroin-based
Janus adhesive dressing
b
SF
SE
200 nm
c
Calcein-labeled
inner layer
Rhodamine B-
labeled Outer layer
Merge
1 μm
1 μm
1 μm
d
SE
SCZ
10 μm
Ca
5 μm
Zn
5 μm
e
SE
2 μm
SCZ
2 μm
f
SF
SCZ
3277.69
3255.71
1514.77
1535.57
4000 3500 3000 2500 2000 1500 1000 500
Wavenumber (cm-1)
g
SF
EGCG
SE1
SE5
SE10
3280
2937
1447
1513
824
1523
4000 3500 3000 2500 2000 1500 1000 500
Wavenumber (cm-1)
h
SF
SE5
SCZ
SCE5
101.98 °C
116.22 °C
126.03 °C
121.78 °C
Heat Flow (w/g)
EXO
50 100 150 200 250
Temperature (°C)

◂**Fig. 1** Characterization of silk fibroin-based Janus adhesive dressing. **a** Preparation process of the Janus adhesive dressing by electrospinning. **b** TEM and **c** CLSM (rhodamine B in the core layer and calcein in the shell layer) images of core–shell/non-core–shell SF electrospun fibers. **d** SEM images of the cross section of the Janus adhesive dressing, and the corresponding EDS elemental mapping of Ca and Zn. **e** SEM images of the surface morphology of the upper layer (SE) and the lower layer (SCZ). **f** FTIR spectra of SF and SCZ. **g** FTIR spectra of SF, EGCG, and SE series (SE_x, x means x% of EGCG). **h** DSC curves of SF, SE_5, SCZ, and SCE_5

electrospinning. The nomenclature and composition ratios of SF with calcium ions (SC), zinc ions (SZ) or calcium/zinc ions (SCZ) in the adherent lower layer are detailed in Table S1, and Table S2 summarizes the EGCG-incorporated core–shell SF fibers (SE_x, x means x% of EGCG) in the upper layer. Table S3 details the upper and/or lower layer architectures for different experimental groups (SF, SCZ, SE_5, SCE_1, SCE_5, and SCE_{10}). As shown in Fig. 1a, the uniform calcium/zinc (Ca^{2+}/Zn^{2+}) modified SF adhesive film (SCZ) was prepared by electrospinning, followed by the preparation of the hydrophilic SF core–shell electrospun fibers (SE) with EGCG encapsulated in the core via coaxial electrospinning based on the SCZ film, to form an all-in-one silk fibroin-based Janus adhesive dressing (SCE). The core–shell structure of the EGCG-loaded SF nanofibers was characterized using transmission electron microscopy (TEM) and confocal laser scanning microscope (CLSM). As shown in Fig. 1b, compared with the uniform contrast of the SF electrospun fiber on TEM image, the contrast between the core and the shell of the SE fibers revealed its coaxial core–shell structure. Moreover, the core and shell layers of the electrospun silk fibroin-based fibers were fluorescently labeled with rhodamine B and calcein, respectively. The CLSM images shown in Fig. 1c exhibit that the core layer emitted red fluorescence and that the shell layer emitted green fluorescence, further confirming the successful fabrication of the core–shell structure by coaxial electrospinning. Compared with single-phase electrospun fibers, the core–shell structure formed by coaxial electrospinning allows for the slow release of the loaded drug in the early stage to meet the phased anti-angiogenetic drug release requirement during wound healing [21, 47].

Next, the morphology of the SCE Janus adhesive dressings was characterized using scanning electron microscope (SEM). The cross section of nanofibers in the upper layer is shown in the upper panel of Fig. 1d, and the vertical views of the upper and lower layer of SCE are shown in Fig. 1e. It can be seen that the nanofibers possess uniform morphology and smooth surface, with average size of nanofibers approximately 1 μm. The lower layer of the SCE Janus adhesive dressings was densely stacked adhesive film enriched with uniformly distributed Ca^{2+} and Zn^{2+} (Fig. 1d). Almost no intact electrospun fibers were observed in the lower layer, which is further supported by the overlay SEM image of SCZ shown in the lower panel of Fig. 1e. Meanwhile, Fourier transform infrared spectroscopy (FTIR) was also employed to characterize pure SF, SCZ, and SE_x (Fig. 1f and g). As shown in Fig. 1f, the characteristic amide I peak at 1636 cm^{-1} and amide II peak at 1514 cm^{-1} for SF, representing C = O stretching and N–H bending respectively, confirming its predominant β-sheet crystalline structure. In contrast, for SCZ, owing to the complexation of Ca^{2+}/Zn^{2+} with carboxyl ($–COO^-$), amino ($–NH_2$), and amide (–CONH–) groups in the SF, the amide II peak in the Ca^{2+}/Zn^{2+}-modified SF shifted to 1535 cm^{-1}. X-ray diffraction (XRD) analysis further confirmed the structural influence of metal ions on SF. As shown in Fig. S1, significant differences were observed between the XRD patterns of the pure SF and SCZ dressing. Compared with pure SF, SCZ exhibited markedly reduced characteristic diffraction peak intensity, indicating decreased crystallinity and confirming successful molecular-level interactions between SF and metal ions. The interaction of SF and metal ions destroys the crystalline structure of SF, thus conferring SCZ with tissue adhesiveness. As shown in Fig. 1g, after being loaded with EGCG, the characterized peak at 824 cm^{-1} from EGCG appeared in the FTIR spectra for all the core–shell electrospun SF with EGCG (SE_1, SE_5, and SE_{10}). The C–N stretching and N–H bending vibrations shifted from 1513 to 1523 cm^{-1}. Concurrently, compared with that of SF, the intensity of the vibrational peak at 1447 cm^{-1}, representing the HO–C stretching peak in SF–EGCG, decreased. These findings suggest that EGCG can interact with SF through hydrogen bonding and hydrophobic interactions, and thus can be firmly incorporated into the inner layers of the core–shell structure, further supporting the gradual and phased release of EGCG. The thermal resistance and stability of silk fibroin-based dressings were characterized using differential scanning calorimetry (DSC) under a nitrogen atmosphere (Fig. 1h). The DSC data reveal that the endothermic peak of SE_5 shifted to 116.22 °C from 101.98 °C for SF, while SCZ exhibited a more obvious shift of 24.05 °C (from 101.98 to 126.03 °C), implying the formation of hydrogen bond network between EGCG's phenolic hydroxyl groups and SF chains. This, along with the incorporation of metal ions, collectively altered the internal structure of SF and significantly enhanced its thermal stability. Furthermore, these thermodynamic properties ensure the structural integrity of the dressing during ambient storage (25 °C) and ethylene oxide sterilization (< 60 °C), providing experimental evidence for the temperature tolerance of silk fibroin-based Janus adhesive dressing.

2.2 Physical, Mechanical, and Release Properties of Silk Fibroin-Based Janus Adhesive Dressing

The water contact angle and water vapor permeability are important indices for evaluating the fluid absorption rate of wound dressings, especially in the context of exudative wounds. The water contact angle and water vapor transmission rate (WVTR) of SF, SCZ, SE_5, SCE_1, SCE_5, and SCE_{10} were measured (Fig. 2a–c). As shown in Fig. 2a and b, both the SF film and SE_5 film (EGCG-loaded core–shell electrospun film) exhibited considerable hydrophilicity, with initial water contact angles of (63.98 ± 11.97)° and (74.65 ± 4.70)°, respectively. After 80 s, the water contact angles for SF and SE_5 films stabilized at (44.43 ± 5.44)° and (47.60 ± 7.13)°, respectively. Previous studies have shown that water contact angles between 40° and 70° are more conducive to the adhesion of epidermal cells and fibroblasts [48]. Therefore, the prepared SCE dressings may support cell adhesion, facilitating cellular ingrowth and wound healing. Furthermore, water droplets were added to the lower layer of the SCE_1, SCE_5, and SCE_{10} bilayer Janus dressings to study the water transport behavior of the film (Fig. 2a). The Ca^{2+}/Zn^{2+}-incorporated SCZ films displayed intrinsic hydrophobicity with initial contact angles of (109.43 ± 16.47)°. This property created a lower hydrophobic/upper hydrophilic structure for SCZ, allowing water to permeate the SE layer through siphon effect, enabling the self-pumping feature of the bilayer Janus dressings. Thus, as a wound dressing, SCE can absorb and transport liquids, promoting wound healing through the absorption of excess exudate. The WVTR measurement reflects the film's ability to allow vapor transmission, which would regulate wound moisture balance. Too high WVTR could lead to excessive wound dehydration, whereas too low WVTR may potentially cause wound pain, bacterial growth, tissue maceration, and dressing detachment. The ideal WVTR value for wound dressings is typically between 2000 and 2500 g/m^2/d (day) to maintain appropriate wound hydration [49]. As illustrated in Fig. 2c, the electrospun nanofiber films, with their high surface area and porosity, led to rapid moisture evaporation, resulting in a WVTR of (5968.12 ± 1032.30) g/m^2/d for SF. During the experiment, the SCZ film ruptured due to its water solubility, resulting in a WVTR as high as (8972 ± 1845.58) g/m^2/d. SE_5 film exhibited significantly reduced WVTR compared to SF film. The SCE bilayer architecture effectively regulated water vapor permeation, and the reduced hydrophilicity of the SE film also hindered water vapor transmission. As the EGCG content increased, the WVTR gradually decreased. The WVTR of SCE_5 was (2221.5 ± 465.42) g/m^2/d, providing favorable conditions to maintain a moist microenvironment for the wound.

Tissue adhesion represents another important feature of dressing, which enables the dressing to adhere stably to the skin defect to protect the wound from external environmental contaminants and hazards, and ultimately facilitate wound repair. The adhesive performance was systematically verified through lap shear and peeling tests. As shown in Fig. 2d, vacuum-dried SCZ exhibited effective and extensive adhesion to substrates such as metal, plastic, glass, and rubber with applied weights up to 100–120 g. The influence of the metal ion content on the adhesive properties of SF was also evaluated. As shown in Fig. 2e, pure SF exhibited negligible tissue adhesiveness, while the incorporation of calcium ions (Ca^{2+}) significantly enhanced the tissue adhesive performance. The SF/Ca^{2+} weight ratio of 70:30 ($SC_{30\%}$ group) led to an optimal lap shear strength against porcine skin as high as (93.48 ± 18.51) kPa. Notably, the $SCZ_{25\%/5\%}$ group with partial substitution of Ca^{2+} with Zn^{2+} preserved comparable adhesive performance comparable to that of the $SC_{30\%}$ group, with a tissue adhesion strength of (94.46 ± 19.47) kPa. Furthermore, peeling tests using the SE upper layer as the substrate and SC films with various SF/Ca^{2+} weight ratios and SCZ as adhesives revealed that under specific humidity, the peel strength initially increased and then decreased as the SF/Ca^{2+} ratio increased from 50:50 to 90:10 (Fig. 2f). The $SC_{30\%}$ group consistently showed superior performance across all concentration gradients, achieving a peel strength of (113.5 ± 17.52) N/m (Fig. 2f), well agreed with the lap shear measurement results. At lower concentrations of Ca^{2+} in SC films (SF/Ca^{2+} ratio > 70:30), amino acids tend to bind with Ca^{2+} rather than form complexes with water molecules [50]. When the SF/Ca^{2+} ratio was in the range of 85:15 to 70:30, the increase in metal complexes and water molecules imparted appropriate viscoelasticity to the SC films, maintaining high energy dissipation and mechanical interlocking, thus leading to high peel strengths. For films with higher concentrations of Ca^{2+} (SF/Ca^{2+} ratio < 70:30), excessive water molecules shielded Ca^{2+} ions, hindering their coordination with amino acids and causing deformation in the structure of SF, reducing both tissue adhesion and peel strength. Notably, when Ca^{2+} was partially substituted by Zn^{2+} (at constant SF/metal weight ratio), the SCZ group exhibited no significant reduction in adhesion or peel strength under the same test conditions. More importantly, the incorporated Zn^{2+}, which serves as an essential component in multiple enzyme systems (including carbonic anhydrase, protein kinase, respiratory enzyme, lactate dehydrogenase, superoxide dismutase, alkaline phosphatase, and DNA/RNA polymerase systems), exerts multifaceted biological effects during wound healing, including antibacterial activity, promotion of fibroblast proliferation, acceleration of ECM synthesis and secretion, and reduction of free radical generation [51]. Consequently, this Ca^{2+}/Zn^{2+} dual-ion modification not only preserves favorable adhesive properties, but also integrates the synergistic biological effects of Ca^{2+} (critical coagulation factor, extracellular

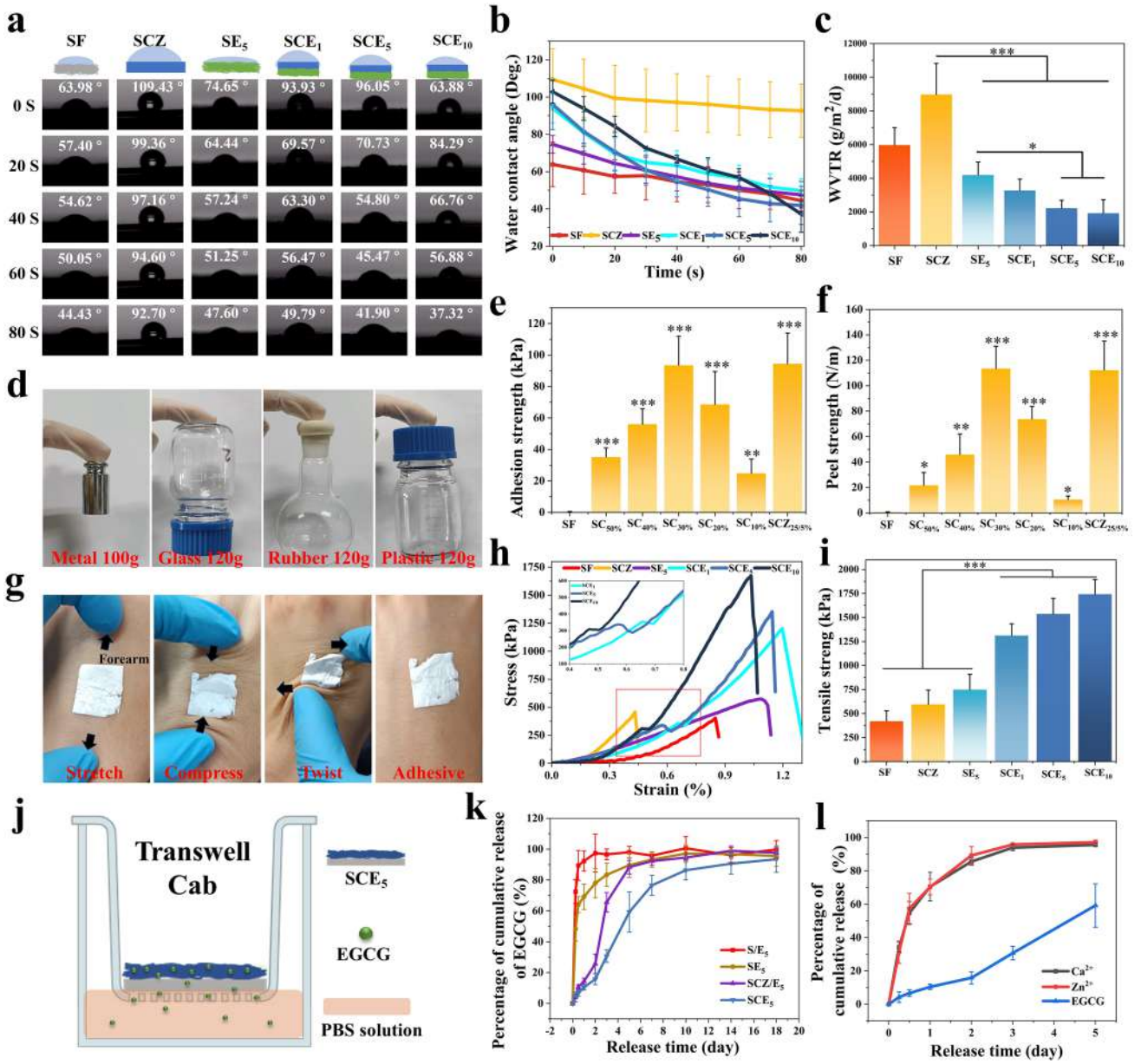

Fig. 2 Physical, mechanical, degradation, and EGCG releasing properties. **a** Photographs and **b** quantitative water contact angle–time curves of different groups ($n=3$). **c** Water vapor transmission rates (WVTRs) of different dressings after 24 h ($n=3$). **d** Adhesion performance of SCZ adhesive against different substrates. **e** Adhesion strengths (measured by lap shear test) against porcine skin of SCZ adhesives with different metal ion ratios ($n=5$). **f** Peel strengths against SE of SCZ adhesives with different metal ion ratios ($n=5$). **g** Photographs of Janus adhesive dressing firmly adhering to the back of the hand under tensile, compressive and torsional forces. **h** The representative stress–strain curves and **i** tensile strengths of different dressings ($n=5$). **j** The setup simulating the phased release of EGCG in practical wound healing application. **k** EGCG releasing curves of different dressings ($n=3$) and **l** Ca^{2+}, Zn^{2+},and EGCG releasing curves for SCE_5 ($n=3$). $^{*}p<0.05$, $^{**}p<0.01$, $^{***}p<0.001$

signaling molecule, and intracellular second messenger in wound healing) and Zn^{2+} [52], potentially enabling significant enhancement of the dressing film's pro-healing efficacy and endowing it with superior potential for scarless wound healing. Thus, SCZ, which incorporated both calcium and zinc ions (denoted as SCZ), was selected as the lower layer of the Janus dressing. The bilayer dressing film was subsequently applied to the back of the hand and subjected to various external forces, such as stretching, compression, and twisting. The SCE dressing film maintained its position without delaminating, tearing, or falling off (Fig. 2g), demonstrating clinical potential for mobile wound sites like joints where conventional dressings fail.

The mechanical properties of the Janus adhesive dressing were studied through tensile stress–strain testing. The results show that the mechanical strengths of the bilayer dressing films were significantly higher than that of the single-layer films (Fig. 2 h and i). The tensile strengths of single-layer films, including pure SF, SCZ, and SE_5, were (420.11 ± 109.25) kPa, (595.29 ± 146.79) kPa, and (748 ± 159.24) kPa, respectively. While, the tensile strengths of the bilayer Janus adhesive dressings, including SCE_1, SCE_5, and SCE_{10}, significantly increased to (1312.45 ± 121.4) kPa, (1537.12 ± 161.22) kPa, and (1743.12 ± 151.67) kPa (Fig. 2i), respectively. As the EGCG content increased, the interaction between EGCG and SF became stronger, resulting in higher strain at break for the SCE Janus adhesive dressings. In addition, obvious fractures in the middle were observed because the lower SCZ layer was more brittle than the upper SE layer (Fig. 2h). In summary, the SCE Janus adhesive dressings showed appropriate tensile strength (1000–2000 kPa) and flexibility for the application as wound dressing in all parts of the body, including areas of dynamic movement and high tension (e.g., knees and elbows).

The sustained and controlled release of bioactive components from wound dressing films is crucial for achieving sequential wound healing microenvironment regulation. According to the design principle, the lower layer of the bilayer dressing film first contacts with the wound tissue and rapidly degrades, followed by the release of active ingredients from the upper layer. First, the degradation of the dressing film was measured by soaking it in PBS. As shown in Fig. S2, SF, and SE films curled up rapidly after contact with the PBS, while the SCZ and SCE films basically maintained their shape. Over time, the solution in the SE group gradually became turbid and appeared to contain film fragments. Meanwhile, the SCZ films gradually degraded, the solution slowly became cloudy, and no film-like substance appeared to be present by the 4^{th} day. However, as the combination of SE and SCZ, SCE initially maintained its basic shape. As the lower SCZ gradually degraded, the entire SCE film began to become transparent, and the solution became turbid. However, unlike in the SCZ group, in the SCE group, the curled-up film structure could be observed on day 7. Therefore, the silk fibroin-based Janus adhesive dressings demonstrated gradient degradation wherein the lower adhesive layer degraded in 3 days, while the upper layer continued degradation, providing the possibility for sequential gradient release of EGCG. Moreover, the Transwell chamber was used to simulate wound interface conditions and evaluate Ca^{2+}, Zn^{2+} and EGCG release behavior (Fig. 2j). Firstly, the release behaviors of the Ca^{2+} and Zn^{2+} from SCZ and SCE (using SCE_5 as the representative) films were measured. As shown in Fig. S3a and b, both SCZ and SCE exhibited synchronous rapid release profiles of Ca^{2+} and Zn^{2+}. Notably, although both SCZ and SCE achieved cumulative release percentages of Ca^{2+} and Zn^{2+} exceeding 93% by day 3, SCZ demonstrated a significantly faster overall release rate than SCE, suggesting that the reverse capillary action of the bilayer dressing might have partially delayed the rapid active ion release from the lower layer. The release kinetics of EGCG from four structurally distinct dressings (monolayer non-core–shell S/E_5, monolayer core–shell SE_5, bilayer non-core–shell Janus adhesive SCZ/E_5, and bilayer core–shell Janus adhesive SCE_5) were systematically determined using UV–vis spectrophotometry. As shown in Fig. 2k and S3c, comparative analysis between representative SE_5 and S/E_5 dressings demonstrated that the non-core–shell S/E_5 nanofibers exhibited characteristic single-phase rapid release, resulting in (92.32 ± 6.48)% EGCG release within 24 h. In contrast, the core–shell SE_5 nanofibers displayed distinct biphasic release behavior, consisting of an initial rapid release phase (69.18 ± 8.23% EGCG released within 24 h) followed by a sustained slow-release phase, ultimately reaching a cumulative release exceeding (93 ± 4.97)% by day 7. These findings clearly demonstrate the regulatory role of core–shell architecture in modulating EGCG release behavior. Release behavior studies of bilayer dressing systems demonstrated that both bilayer non-core–shell fiber dressings (SCZ/E_5) and bilayer core–shell fiber dressings (SCE_5) exhibited significantly delayed EGCG release because of the effective water penetration barrier provided by the lower SCZ layer. During the initial phase, only a small amount of EGCG physically adsorbed or weakly bound to SF nanofibers was released, resulting in less than 26% cumulative release within 48 h. As the experiment progressed, degradation of the lower SCZ layer enabled direct contact of the upper EGCG-loaded layer with the degradation medium, resulting in accelerated release rate. However, the EGCG release from SCZ/E_5 dressings persisted for approximately 14 days due to diffusion limitation effects and inherently slow degradation kinetics of SF nanofibers. Notably, the SCE_5 dressing, with the core–shell structure, displayed a significantly prolonged EGCG release duration (exceeding 18 days) owing to its unique drug encapsulation core–shell architecture, conclusively demonstrating the regulatory role of material structural design in controlling drug release kinetics. Meanwhile, comparative analysis of the release kinetics among the three active components (EGCG, Ca^{2+}, and Zn^{2+}) in SCE_5 dressings revealed that both Ca^{2+} and Zn^{2+} achieved cumulative release rates exceeding 85% by day 2, while EGCG started its rapid release phase from day 2 (Fig. 2i). This differential release behavior further demonstrated that the dressing can achieve stage-specific functional regulation through the sequential release of different active components. In summary, the above results demonstrate that by using the macro bilayer and micro core–shell dual design, the initial burst release of EGCG is reduced and

the sustained EGCG release curve is extended, allowing the release of EGCG to be controlled for more than 14 days. This enables an initial slow and phased release of EGCG, supporting the early-phase small amount of EGCG release to exhibit anti-inflammatory and antioxidant effects beneficial for wound healing, followed by the continuous release of a substantial amount of EGCG in the later wound healing phases to prevent excess angiogenesis.

2.3 Biocompatibility of Silk Fibroin-Based Janus Adhesive Dressing

Ideal skin wound dressings often need to possess high biocompatibility [53]. The cytotoxicity of EGCG was firstly evaluated using both mouse fibroblasts (L929) and human umbilical vein endothelial cells (HUVEC) as cell models (Fig. S4). It can be seen that L929 still maintained a high cell viability of (91.30 ± 4.49)% at an EGCG concentration up to 200 μg/mL. While, compared with that of L929 cells, the cell viability of HUVEC cells at 200 μg/mL EGCG significantly decreased to (67.13 ± 6.84)%. The cytotoxicity tests using extracts of the core–shell SE at various ratios were also conducted. As shown in Fig. S5, the results of the CCK-8 assay reveal that the survival rate of L929 cells in the SE_{10} group exceeded 80%, which was greater than that in the other groups. Compared with L929 cells, HUVEC cells exhibited higher dose-dependent sensitivity to EGCG.

Subsequently, based on the results of the adhesion and peeling experiments (Fig. 2 e and f), the SF/metal ion ratio (70:30) with the best adhesive performance was selected for adjusting Ca^{2+}/Zn^{2+} ions ratios at different formulations. The results in Fig. S6 show that excessively elevated Zn^{2+} ratios severely compromised cell viability, while the 25:5 Ca^{2+}/Zn^{2+} ratio optimized Zn^{2+} bioavailability while maintaining (105.00 ± 7.54)% cell viability. Therefore, an SF/Ca^{2+}/Zn^{2+} ratio of 70:25:5 was selected for the adhesive layer and SE_1, SE_5, and SE_{10} for the core–shell layer in the preparation of the Janus adhesive dressings. Following GB/T 16886.1–2022 "Biological Evaluation of Medical Devices", extracted leachates from SF, SCZ, SE_5, SCE_1, SCE_5, and SCE_{10} were subjected to CCK-8 cytotoxicity tests using L929 and HUVEC cells. As depicted in Fig. 3a and b, none of the groups exhibited significant toxicity, and the SCE Janus adhesive dressings promoted cell proliferation. After co-culturing the material extracts with L929 cells, the CCK-8 assay and Live/Dead cell staining revealed continuous and steady cell proliferation across all the groups over time (Fig. 3c and d). Only SCE_{10} exhibited partial cytotoxicity with cell proliferation rate of (489 ± 61.74)% on day 3. The cell proliferation rates were lower in the SCZ (891.75 ± 114.81%) and SE_5 (841.61 ± 45.51%) groups than in the control group (937.81 ± 71.32%), but the proliferation rate in the SCE_1 (1021.75 ± 128.43%) and SCE_5 (960.96 ± 84.05%) was greater than that in the control group. In summary, the dressings demonstrated excellent biocompatibility, significantly promoting cell proliferation. The dressings did not induce cytotoxicity or adverse effects on the target wound. On the contrary, the SCE Janus adhesive dressings were more conducive to cell proliferation.

The cell scratch assay is currently the most commonly used method for evaluating cell migration and repair capabilities. In vitro scratch assays (Fig. 3e and f) demonstrated significantly different cell migration rates between SCE_5 and the control group after 48 h ($p < 0.05$). The cell migration rates in the SCE_1 and SCE_5 groups were notably higher than those in the blank group, reaching approximately (64.28 ± 3.57)% and (65.00 ± 7.63)%, respectively, within 48 h. Although the migration rates in the SF, SCZ, and SE_5 groups were also greater than those in the control group, which showed only a (46.83 ± 3.79)% migration rate. In contrast, the cell migration rate in the SCE_{10} group, with a high EGCG content, was significantly inhibited ($p < 0.05$), suggesting that a higher EGCG load may adversely affect cell activity and consequently impair cell migration. To further validate the migration-promoting properties of the Janus adhesive dressings, the Transwell experiment was conducted. As shown in Fig. 3 g and h, the results of crystal violet staining of cells on the lower surface of the chamber were consistent with the results of the scratch assay. Significant differences in cell migration rates were observed between the SCE_5 and the control group ($p < 0.05$). Both SCE_1 and SCE_5 significantly promoted directional cell migration, with SCE_5 showing maximal efficacy. Among all the Janus adhesive dressings, the bilayer Janus adhesive dressings showed higher cell migration than the single-layer Janus adhesive dressings, likely due to the complementary properties of the layers and the controlled release of metal ions and EGCG during extraction. However, as the EGCG ratio in the bilayer Janus adhesive dressing increased to 10 mg/mL, the cytotoxicity of the dressing also increased. Direct cytotoxicity tests of EGCG, as shown in Fig. S4, revealed that cell activity was significantly inhibited at concentrations above 200 μg/mL. Consistent with this, based on the EGCG content measured in the release experiments (Fig. S7), the total concentration in the SCE_{10} group was significantly higher than 200 μg/mL in the same area of the dressing, further confirming that EGCG is effective only within specific concentration ranges.

2.4 Anti-inflammatory and Antioxidant Properties of Silk Fibroin-Based Janus Adhesive Dressings

At the wound site, excessive accumulation of ROS often leads to oxidative stress, resulting in lipid peroxidation, DNA damage, and enzyme inactivation, which are detrimental to wound healing. Reducing the level of oxidative stress

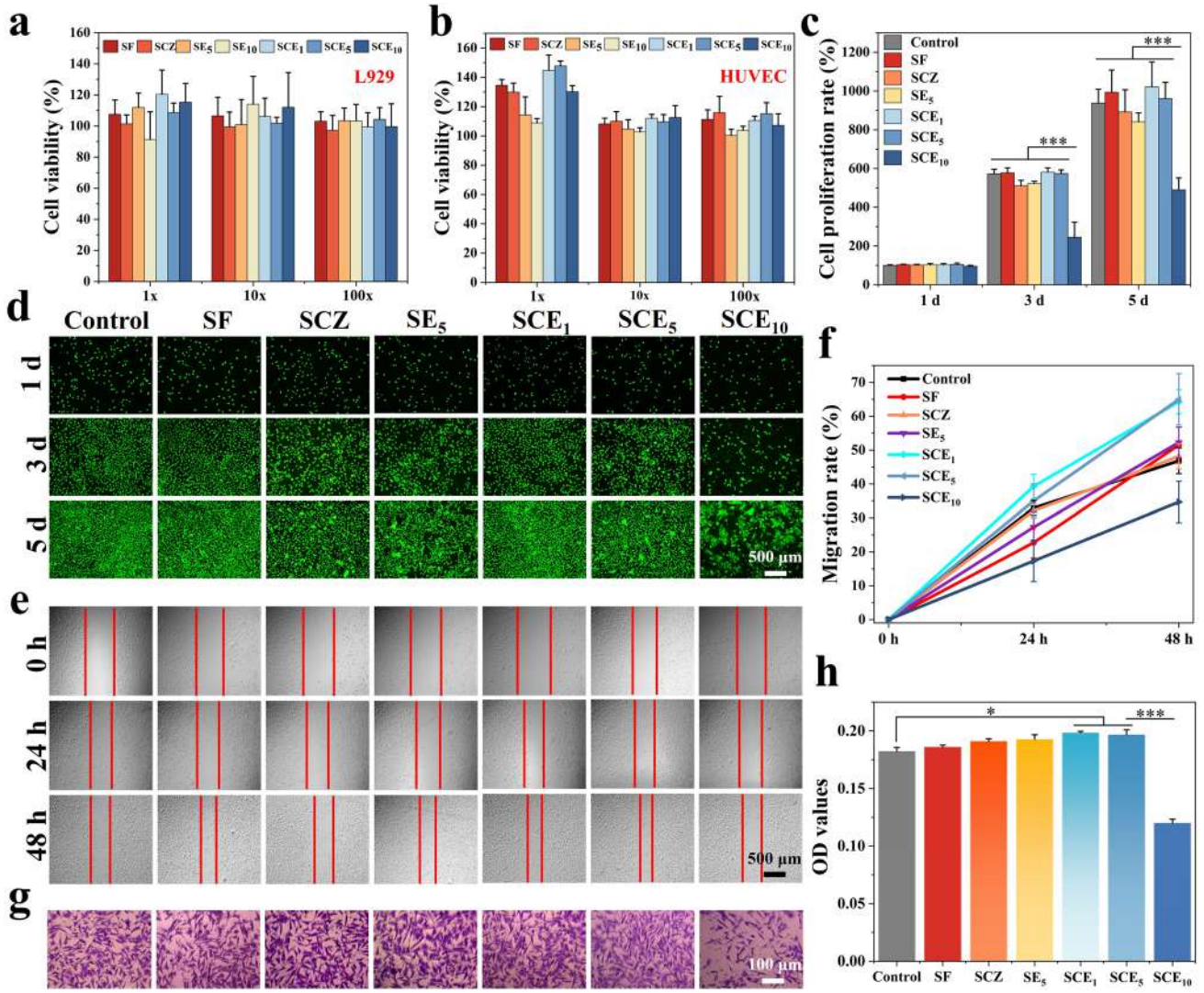

Fig. 3 Cytocompatibility evaluation. Cell viability of **a** L929 and **b** HUVEC cells after co-culturing with the extraction solutions of different samples at different dilutions for 24 h ($n=4$). **c** The CCK-8 absorbances and **d** the Live/Dead staining images of L929 cells after proliferation for 1, 3, and 5 days in the presence of the 1 × extraction solutions of different samples ($n=3$). **e** Typical microscopic images of L929 cells in a scratch assay (1 × extraction solution) and **f** quantitative migration rates for different groups ($n=3$). **g** Photographs of the transwell migration of crystal violet-stained L929 cells in the presence of 1 × extraction solution of different samples and **h** the quantitative OD values ($n=3$). $^{*}p<0.05$, $^{**}p<0.01$, $^{***}p<0.001$

in wounds favors the prognostic outcome [54]. The antioxidant capacity of the Janus adhesive dressings was evaluated by assessing their ability to scavenge stable 1,1-diphenyl-2-picrylhydrazyl (DPPH) free radicals (Fig. 4a), intracellular ROS, and inflammatory factors (Fig. 4b). Quantitative analysis in Fig. 4c and d demonstrates that SF and SCZ films exhibited limited DPPH radical scavenging capacity, with < 20% free radical clearance efficiency. After loading with EGCG, the DPPH absorption peak at 516 nm significantly reduced. Within 30 min, the SCE_1 group achieved a (46.10 ± 7.90)% scavenging rate. Dose-dependent scavenging kinetics were observed, with the SCE_5 and SCE_{10} films showing scavenging rates of (69.02 ± 1.31)% and (84.75 ± 4.02)%, respectively. The efficiency of the SCE_5 film in scavenging free radicals was then measured over different periods. Results demonstrate that despite the initial core–shell structure hindered the release of EGCG, the SCE_5 still achieved a scavenging rate of (85.80 ± 0.79)% for DPPH within 60 min (Fig. 4 e and f). Furthermore, the intracellular ROS scavenging capacity of the dressings was assessed using H_2O_2-induced oxidative stress model in L929 cells. As shown in Fig. 4g, after being treated with EGCG-loaded dressings, including SE_5, SCE_1, SCE_5 and SCE_{10}, the L929 cells with high intracellular ROS exhibited much weaker 2',7'-dichlorodihydrofluorescein (DCF) fluorescence (green) compared to the control, SF, and SCZ groups. The SCE_1,

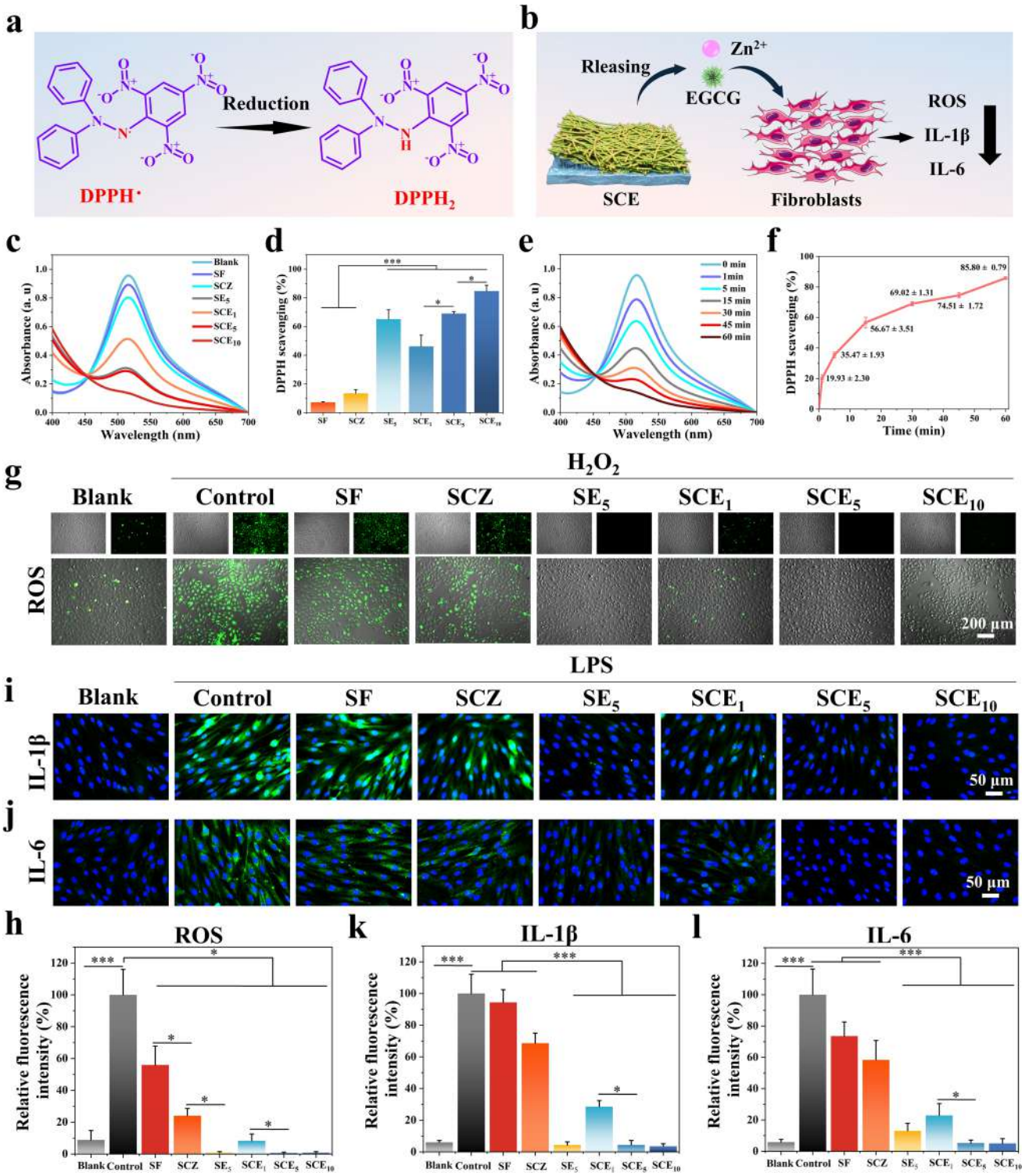

Fig. 4 Antioxidant and anti-inflammatory activity. **a** Schematic diagram of the reduction reaction of DPPH. **b** Schematic diagram of the anti-inflammatory effect of SCE and possible mechanism. **c** UV–Vis curves and **d** corresponding DPPH scavenging percentages after 30 min incubation with different samples ($n=3$). **e** UV–Vis curves and **f** the dynamic change of DPPH scavenging percentages for SCE_5 ($n=3$). **g** The fluorescence images and **h** relative fluorescence intensities reflecting intracellular ROS levels of L929 cells after being treated with the 1 × extraction solution of different samples ($n=3$). The **i** IL-1β and **j** IL-6 immunofluorescence staining images and the relative fluorescence intensities of **k** IL-1β and **l** IL-6 for different samples ($n=3$). $^{*}p<0.05$, $^{**}p<0.01$, $^{***}p<0.001$

SCE_5, and SCE_{10} groups showed fluorescence intensities of (8.29 ± 4.26)%, (0.63 ± 0.55)% and (0.80 ± 0.62)% of that in the control group respectively (Fig. 4h), further confirming the excellent antioxidant activity of the silk fibroin-based Janus adhesive dressing. Then the anti-inflammatory activity of the dressings was evaluated by measuring the levels of inflammatory factors in fibroblasts stimulated with lipopolysaccharide (LPS). Interleukin-1β (IL-1β) and interleukin-6 (IL-6) are potent pro-inflammatory cytokines that affect various cell types and are produced by T cells, macrophages, and fibroblasts [55]. As shown in Fig. 4i and j, the addition of LPS significantly increased the expression levels of IL-1β and IL-6 in fibroblasts. Due to the anti-inflammatory activity of Zn^{2+}, the fluorescence intensity of IL-1β and IL-6 was weaker in the SCZ group than in the control and SF groups, with the relative fluorescence intensity of IL-1β and that of IL-6 being (68.60 ± 6.38)% and (58.32 ± 12.40)% to that in the control group (Fig. 4k and l), respectively. The presence of the main anti-inflammatory agent EGCG significantly reduced the intracellular levels of IL-1β and IL-6. For the SCE_1 group, which contained only a small amount of EGCG, the relative fluorescence intensity of IL-1β decreased to (28.55 ± 3.76)%, and that of IL-6 decreased to (22.91 ± 7.48)% of that in the control group (Fig. 4k and l). For SE_5, SCE_5, and SCE_{10} with higher levels of EGCG, the relative fluorescence intensity of IL-1β was less than 5%, and the relative fluorescence intensity of IL-6 was less than 13% of that in the control group. These findings demonstrate that EGCG-incorporated dressings potently scavenge intracellular ROS and suppress pro-inflammatory cytokine secretion, collectively contributing to potent anti-inflammatory efficacy.

2.5 Angiogenesis Regulation Properties of Silk Fibroin-Based Janus Adhesive Dressings

During the wound healing process, neovascularization occurs in the proliferation phase to support tissue reconstruction. However, in the remodeling phase, these blood vessels often undergo functional degradation and gradual occlusion and are eventually replaced by newly formed collagen fibers [56]. Mounting evidence indicates that uncontrolled angiogenesis due to excessive inflammatory responses, or the degeneration of damaged vessels, can affect wound healing, leading to scar formation and tissue dysfunction [38]. Properly regulating, rather than just promoting, angiogenesis during wound repair may facilitate better reconstruction of skin tissue and lead to more favorable long-term healing outcomes. The anti-angiogenic capacity of the Janus adhesive dressings was evaluated through the tube formation assay (Fig. 5a) and by detecting the expression of platelet endothelial cell adhesion molecule-1(CD31) and VEGF (Fig. 5b). As shown in Fig. 5 c and d, in the HUVEC cells tube formation assay, many mature tubular structures were formed in the control, SF, and SCZ groups, with no significant statistical differences in the relative tube length of tubular networks among these three groups. In the groups of films loaded with EGCG, as the amount of EGCG increased, the tubular structures became shorter and incomplete, with the relative tube length of SCE_5 of only (34.07 ± 10.80)% ($p < 0.001$) compared to the control group. Subsequently, the anti-angiogenic ability of the Janus adhesive dressings was assessed by detecting CD31 and VEGF expressions in HUVEC cells. As shown in Fig. 5e and f, high level expressions of both CD31 and VEGF were observed in the control, SF, and SCZ groups, while along with the increase of EGCG, the CD31 expression levels of the SE_5, SCE_1, SCE_5, and SCE_{10} groups were significantly suppressed to (12.17 ± 2.53)%, (73.92 ± 8.22)%, (9.80 ± 1.69)%, and (7.55 ± 1.54)% of that in the control group (Fig. 5g, $p < 0.05$), respectively, and the VEGF expression levels were also decreased to (10.31 ± 6.19)%, (63.13 ± 5.15)%, (7.58 ± 4.52)%, and (4.99 ± 3.36)% to that of the control group (Fig. 5h, $p < 0.05$), respectively. These results indicate that high-dose EGCG loading can significantly reduce pro-angiogenic factor production, thereby inhibiting angiogenesis, which is conducive to preventing scar tissue formation in the late stage of wound healing [45].

2.6 Antibacterial Activity of Silk Fibroin-Based Janus Adhesive Dressing

Antimicrobial activity represents one of the critical properties of wound dressings that promotes wound healing by inhibiting bacterial proliferation and reducing infection risk. Representative Gram-positive (*Staphylococcus aureus*, abbreviated as *S. aureus*) and Gram-negative (*Escherichia coli*, abbreviated as *E. coli*) bacteria were selected to evaluate the antibacterial performance of SCE dressings. As shown in Fig. 6 a and b, the plate culture experiments demonstrated that the SCZ, SE, SCE_1, SCE_5, and SCE_{10} derssings exhibited gradually enhanced antibacterial activity compared to that of the control and SF dressing groups. Specifically, as shown in Fig. 6c, the bacterial survival ratios of *S. aureus* were (39.39 ± 8.18)% for SCZ and (51.52 ± 9.35)% for SE_5, while their combination SCE_5 showed significantly enhanced antibacterial effect (bacterial survival ratio = 3.54 ± 1.27%). Figure 6d reveals a similar trend in antibacterial activity against *E. coli*, in that the antibacterial efficacy displayed a distinct dose-dependent enhancement with increasing EGCG content in the SCE formulations (SCE_1, SCE_5, and SCE_{10}), unequivocally demonstrating the crucial role of EGCG in conferring antimicrobial ability to the materials. Consequently, the SCE dressing demonstrated pronounced antibacterial properties attributable to the synergistic

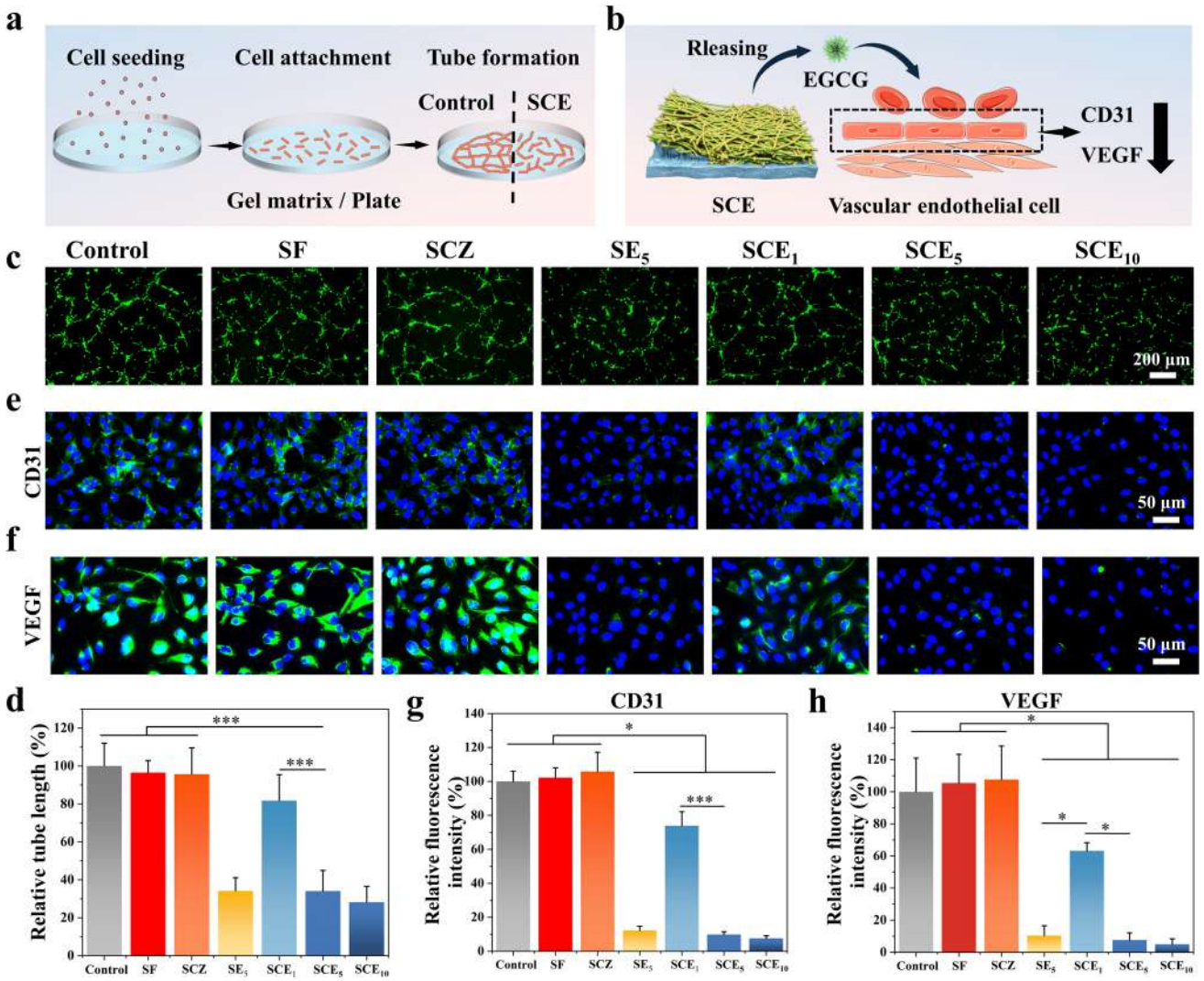

Fig. 5 Angiogenesis inhibition effect evaluation. **a** Schematic diagram of tube formation assay, and **b** angiogenesis inhibition effect of SCE by releasing EGCG. **c** Fluorescent images of tube formation assay and **d** the relative tube lengths after HUVEC cells being treated with the 1 × extraction solution of different samples ($n = 3$). **e** CD31 and **f** VEGF immunofluorescence staining images and the relative fluorescence intensities for **g** CD31 and **h** VEGF after being treated with the 1 × extraction solution of different samples ($n = 3$). $^{*}p < 0.05$, $^{**}p < 0.01$, $^{***}p < 0.001$

coordination between Ca^{2+}/Zn^{2+} ions and EGCG (Fig. 6e). This antimicrobial efficacy ensures that the dressing can effectively mitigate wound infection risks while establishing a pro-regenerative microenvironment to enhance repair of full-thickness skin wounds.

2.7 In Vivo Hemostatic Capacity of Silk Fibroin-Based Janus Adhesive Dressing

Full-thickness skin wounds often cause unavoidable bleeding. Dressings possessing rapid hemostatic capacity play a crucial role in the initial phase. Rat liver incision model and rat tail model was established to evaluate the hemostatic ability of the SCE Janus adhesive dressings. As shown in Fig. 6 f and g, the blood loss from the liver in the control group reached approximately (0.53 ± 0.15) g, while the blood loss in the SCZ group was (0.21 ± 0.09) g. In contrast, the blood loss was only (0.18 ± 0.08) g in the SCE_5 group, indicating significant differences in blood loss among the groups. In the rat tail model of Fig. 6 h and i, the bleeding volume of the blank group was significantly higher than that in the SCE_5 group, with blood losses of (0.28 ± 0.08) g, (0.09 ± 0.04) g, and (0.09 ± 0.03) g in the control, SCZ, and SCE_5 groups, respectively. These results indicate that the

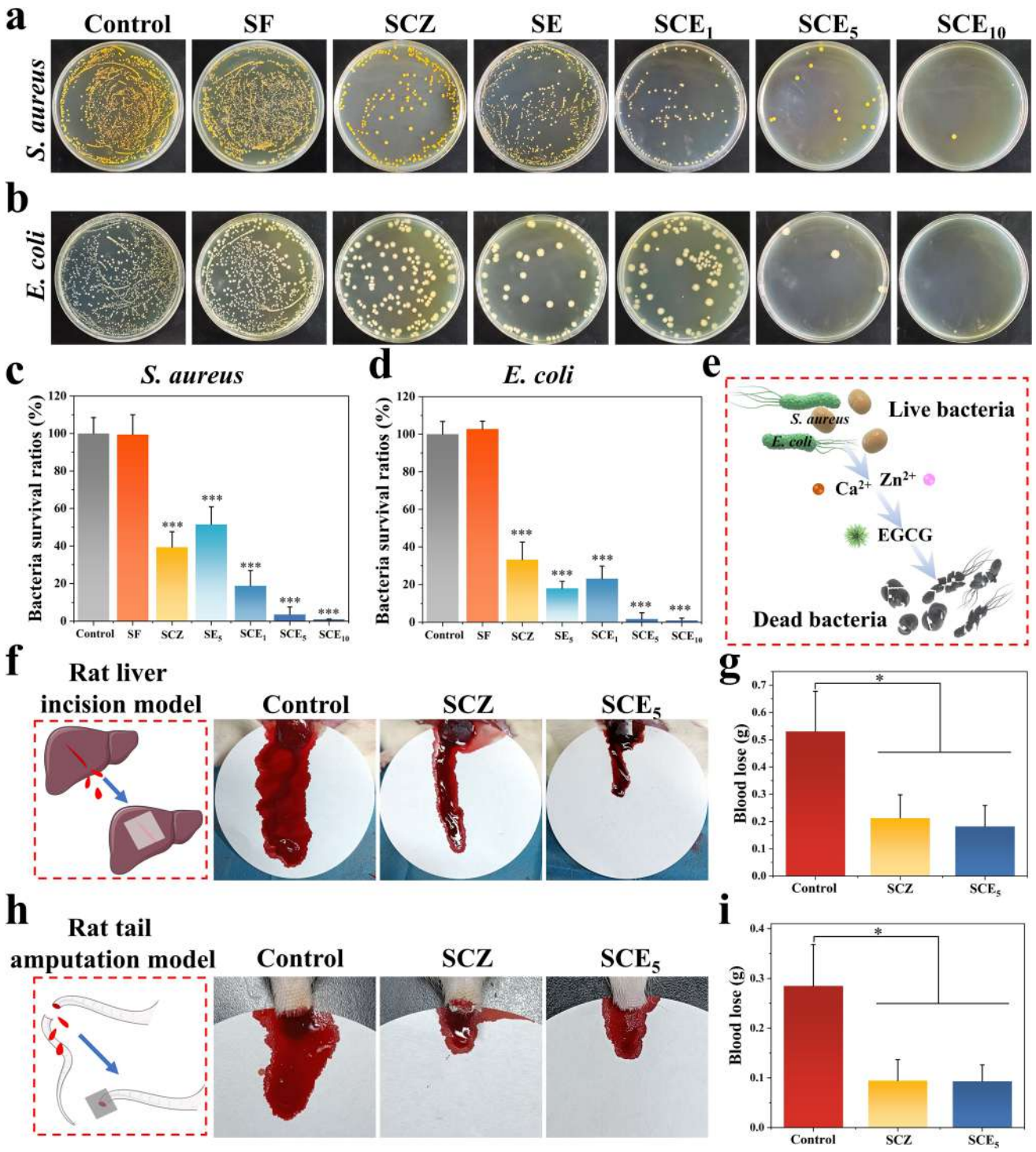

Fig. 6 Antibacterial activity and hemostatic properties. The photographs of survival bacterial colonies of **a** *S. aureus* and **b** *E. coli*. The bacterial survival ratios of **c** *S. aureus* and **d** *E. coli* ($n=3$). **e** Schematic diagrame of the possible antibacterial mechanism of the SCE. **f** Schematic diagram and hemostatic photographs using rat liver incision model, and **g** blood loss amounts for different groups ($n=3$). **h** Schematic diagram and hemostatic photographs using rat tail amputation model, and **i** blood loss amounts for different groups ($n=3$). $^{*}p<0.05$, $^{**}p<0.01$, $^{***}p<0.001$

SCE Janus adhesive dressings exhibit effective hemostatic capacity in vivo, which might be attributed to the high concentration of Ca^{2+} in its adhesive layer.

2.8 Verification of Rat Full-thickness Wound Healing Effect in Rats

To further assess the application of the bilayer Janus adhesive dressings in wound healing, a full-thickness skin wound repair experiment was conducted in rats to confirm the potential of the SCE Janus adhesive dressings in promoting wound healing and inhibiting scar formation. SF, SCZ, SE_5, SCE_5, and SCE_{10} were chosen as the material groups, with an untreated group served as the control. As shown in Fig. 7a and b, serial wound healing progression was evaluated through photographic documentation of rat wounds and quantitative analysis of dorsal wound diameters on days 0, 3, 7, 14, and 21. In terms of the overall trend, the SCE_5 group showed a faster wound contraction than that of the control groups ($p < 0.05$). By day 7, the wound healing rate in the SCE_5 group was (56.40 ± 5.77)%, already showing a significant healing promotion ability compared with other groups. By day 14, the wounds in the SCE_5 group almost completely healed, with a wound healing rate of (86.81 ± 1.19)%. In contrast, the wounds in the other five groups showed varying sizes, among which the control group having the largest unhealed wound area with a wound closure ratio only of (53.36 ± 4.44)%. By day 21, all groups showed nearly completely wound healed except for the control group, the wound closure rate of which was only (80.59 ± 8.47)%. These results indicate that the application of the SCE Janus adhesive dressings can improve and accelerate wound healing.

To better evaluate the effects on wound healing, a histological analysis of the rat wounds was conducted. As shown in Fig. S8, all groups exhibited various degrees of inflammatory cell infiltration and fibroblast migration and proliferation, along with some degree of re-epithelialization on day 7. Compared with the other five groups, the SCE_5 group presented a more extensive epithelial tongue extension, fibroblast migration and angiogenesis. By day 14, the control, SF, and SCZ groups lacked complete dermal tissue formation, whereas the SE_5, SCE_5, and SCE_{10} groups showed full epidermal coverage and complete dermal tissues formation. Among them, the SCE_5 group showed the highest degree of re-epithelialization, with a few skin appendage structures observed in the skin tissue. By day 21, with the exception of the control group, all the other groups showed complete re-epithelialization. The wounds in the SCE_5 group most closely resembled normal skin tissue, with hair follicles and sebaceous glands visible in the newly formed tissue at the wound site (Fig. 7c). The wounds in the other groups and the control group mostly exhibited collagen fiber deposition and occasional incomplete appendage structures, indicating that their skin tissue outcome was scar healing without significant regeneration. Quantitative measurements of scar width for each group on day 21 (Fig. 7d) reveal that the scar widths for the control, SF, SE, SE_5, and SCE_{10} groups were (5.22 ± 0.87) mm, (3.63 ± 0.95) mm, (3.00 ± 0.94) mm, (2.13 ± 0.66) mm, and (2.51 ± 0.43) mm, respectively. Notably, the SCE_5 group exhibited the narrowest scar formation (0.62 ± 0.15 mm). These results further demonstrate that SCE_5 significantly inhibited scar formation.

Collagen deposition is a key factor determining the strength and appearance of the skin. Thus, Masson's trichrome staining (MTS) was used to evaluate collagen deposition and fibrosis extent. As shown in Fig. 7e, f and S8, collagen metabolism continuously changed throughout the healing process. On day 7, based on the intensity and area of blue MTS staining, there were no significant differences in collagen depositions among the six groups. From day 7 to day 14, the collagen content gradually increased in each group, with the highest value in the control group, which reached (54.14 ± 2.39)% of collagen volume fraction. In contrast, the EGCG-loaded groups, including the SE_5, SCE_5, and SCE_{10} groups, presented significantly less collagen depositions than that of the control group ($p < 0.05$). By day 21, the difference intensified, with the lowest collagen content in the SCE_{10} group, followed by the SCE_5 group. This difference could be attributed to EGCG, which inhibits angiogenesis during the later stages of wound healing, thereby further suppressing collagen deposition. Additionally, Sirius Red staining was used to assess the anti-scarring potential of the SCE Janus adhesive dressings. Type I collagen is typically considered a prominent component of the extracellular matrix in HS, with a higher proportion of type I/III collagen in HS than in normal skin. As shown in Fig. 7 g, h and S9, the ratio of type I (red) to type III (green) collagen showed little variation among the groups on day 14. After 21 days, the ratio of type I/III collagen was lower in the SCZ, SE_5, SCE_5 and SCE_{10} treatment groups than in the control group ($p < 0.05$), with the lowest ratio in the SCE_5 group (Fig. 7h). This finding indicates that the SCE_5 group exhibited the minimal scar formation, with Sirius Red staining images most closely resembling those of normal skin tissue. Concurrently, quantitative analysis of collagen fiber alignment was conducted in rat wound repair tissues. The results (Fig. S10) revealed significant inter-group variations in collagen fiber organization: both the control and SF groups exhibited an unidirectional alignment pattern, but the SCE-treated group demonstrated spatial distribution characteristics that more closely approximated the multidirectional basket-weave architecture characteristic of normal skin tissue. In addition, hydroxyproline was used as an additional indicator to evaluate healed skin tissue. Hydroxyproline is an important component of collagen fibers, with a constant

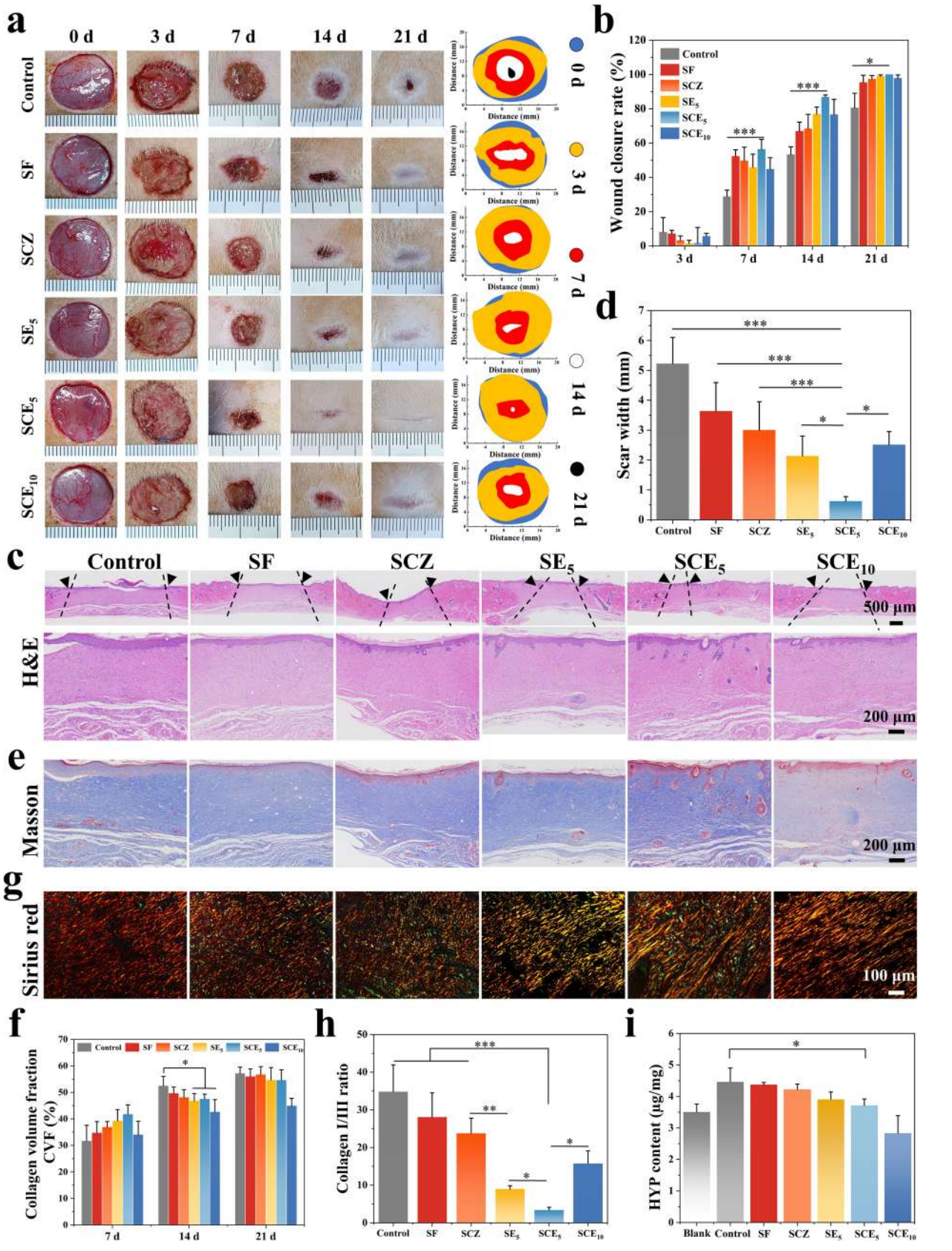
a
0 d
3 d
7 d
14 d
21 d
Control
SF
SCZ
SE5
SCE5
SCE10
Distance (mm)
b
Wound closure rate (%)
Control
SF
SCZ
SE5
SCE5
SCE10
3 d
7 d
14 d
21 d
d
Scar width (mm)
c
H&E
500 μm
200 μm
e
Masson
200 μm
g
Sirius red
100 μm
f
Collagen volume fraction CVF (%)
h
Collagen I/III ratio
i
HYP content (μg/mg)
Blank

◂**Fig. 7** In vivo assessment using a full-thickness wound model on SD rats. **a** Representative photographs of the wounds treated with different samples on days 0, 3, 7, 14, and 21, and **b** the calculated wound closure rates ($n=5$). **c** H&E staining images of skin tissue on day 21 of the treated wounds (black dotted line: edge of wound scar), and **d** the measured scar widths ($n=5$). **e** Masson's trichrome staining images of the treated wound tissues on day 21 and **f** the collagen volume fractions of different groups on day 7, 14, and 21 ($n=5$). **g** Sirius Red staining images of the treated wound tissues on day 21, and **h** the calculated collagen I/III ratios (n = 5). **i** Hydroxyproline (HYP) contents of the treated wound tissues on day 21 ($n=5$). $^{*}p<0.05$, $^{**}p<0.01$, $^{***}p<0.001$

mass fraction in collagen at 13.4% [57]. Therefore, hydroxyproline is widely used to assess the content and quality of collagen fibers. The deposition of collagen in the skin tissue after wound healing was assessed in each group by measuring the hydroxyproline content. As shown in Fig. 7i, the hydroxyproline content in the SE_5, SCE_5, and SCE_{10} groups, containing EGCG, was significantly lower than that in control group ($p<0.05$). This result is consistent with the trend of the results shown in Fig. 7e and f. Together, these results demonstrate that the SCE Janus adhesive dressings reduce excessive collagen deposition during the late wound healing phase, resulting in a healed skin tissue texture that more closely resembles normal skin tissue.

2.9 Expression of Inflammatory Factors, Transforming Growth Factors, and Vascular-Related Expression Factors in Wound Healing

To further confirm the anti-inflammatory, angiogenesis modulating, and regenerative effects of the silk fibroin-based Janus adhesive dressings on rat wounds, histological staining was performed for IL-1β, Interleukin-10 (IL-10), TGF-β and platelet endothelial cell adhesion molecule-1/α-smooth muscle actin (CD31/α-SMA). Interleukins play important roles in the inflammatory response by signal transduction, immune cell activation and regulation, and T/B cell activation, proliferation, and differentiation [58]. IL-1β is overexpressed in local tissues, leading to fever, inflammation, and pathological changes in certain diseases. As shown in Fig. 8 a and b, the control group presented the highest IL-1β expression level (set as $100\pm10.47\%$) on day 7, while the SCE_5 group exhibited significantly lower IL-1β expression ($35.85\pm5.78\%$, $p<0.001$). The other experimental groups also displayed varying degrees of IL-1β downregulation, with values at $(91.89\pm3.59)\%$, $(70.56\pm11.89)\%$, $(43.19\pm10.91)\%$ and $(62.35\pm5.31)\%$ in the SF, SCZ, SE_5 and SCE_{10} groups, respectively. By day 14, although IL-1β expression decreased across all groups compared with that on day 7, the control group still maintained the highest expression levels (Fig. S11a). Notably, IL-1β expression in the SCE_5 group decreased to nearly undetectable levels, indicating that the SCE dressing film significantly reduced pro-inflammatory cytokine expression and exerted sustained anti-inflammatory effects. IL-10 is a classic anti-inflammatory and immunosuppressive factor that regulates cell growth and differentiation and modulates inflammatory and immune responses [59]. Assessment of IL-10 expression in the treated wound tissues would further validate the anti-inflammatory efficacy of the Janus dressing. As shown in Fig. 8 c and d, IL-10 expression exhibited an inverse trend compared with IL-1β on day 7 post-surgery. The SCE_5 group presented the highest IL-10 levels ($242.44\pm20.03\%$ of the control, $p<0.001$), followed by the SE_5 group, while the control group showed the lowest IL-10 expression. By day 14, the control group maintained persistently elevated IL-10 levels without significant reduction (Fig. S11b), indicating a sustained inflammatory status in these wounds. Notably, the SCE_5 group showed no significant IL-10 expression, suggesting the successful transition from the inflammation phase to the proliferation phase in SCE_5 treated wounds. Combined with the results of IL-1β expression (Fig. 8 a, b and S11a), these findings suggest that SCE_5 attenuates the inflammatory response by decreasing the expression of pro-inflammatory factors and increasing the expression of anti-inflammatory factors. This facilitates a faster transition from the inflammation phase to the proliferation phase, promoting wound re-epithelialization. The better anti-inflammatory effect of SCE_5 than that of SE_5 may be due to the synergistic effect of Zn^{2+} in the adhesive layer enhancing the anti-inflammatory effect. In the SCE_{10} group, excessive EGCG may exhibit biotoxicity, potentially delaying tissue repair.

TGF-β is widely regarded as a key regulatory factor in skin wound repair. It promotes the recruitment of inflammatory cells and increases the expression of genes related to ECM formation (including fibronectin) to initiate granulation tissue formation, thereby promoting fibroblast proliferation, migration, and wound healing [60]. However, excessive expression of TGF-β can increase fibrosis, alter the progression of wound healing, and promote scar formation [6]. As shown in Fig. 8 e and f, TGF-β expression in the SCE_5 group peaked ($21.02\pm3.61\%$) on day 7 and then gradually decreased on days 14 and 21. TGF-β expression in the control group was initially low ($2.21\pm1.69\%$), increased on day 14, and then decreased on day 21, showing a trend almost opposite to that in the SCE_5 group. The SCZ and SCE_{10} groups presented similar trends in terms of TGF-β expression, with higher expression than in the SF and control groups on day 7 but lower expression than in the SCE_5 group, followed by an initial increase and subsequent decrease. The trend in the SE_5 group was similar to that in the SCE_5 group, but the expression of TGF-β was higher than that in the SCE_5 group on days 14 and 21. TGF-β exhibits time-dependent effects, with stage-specific expression patterns that influence final healing outcomes. Thus,

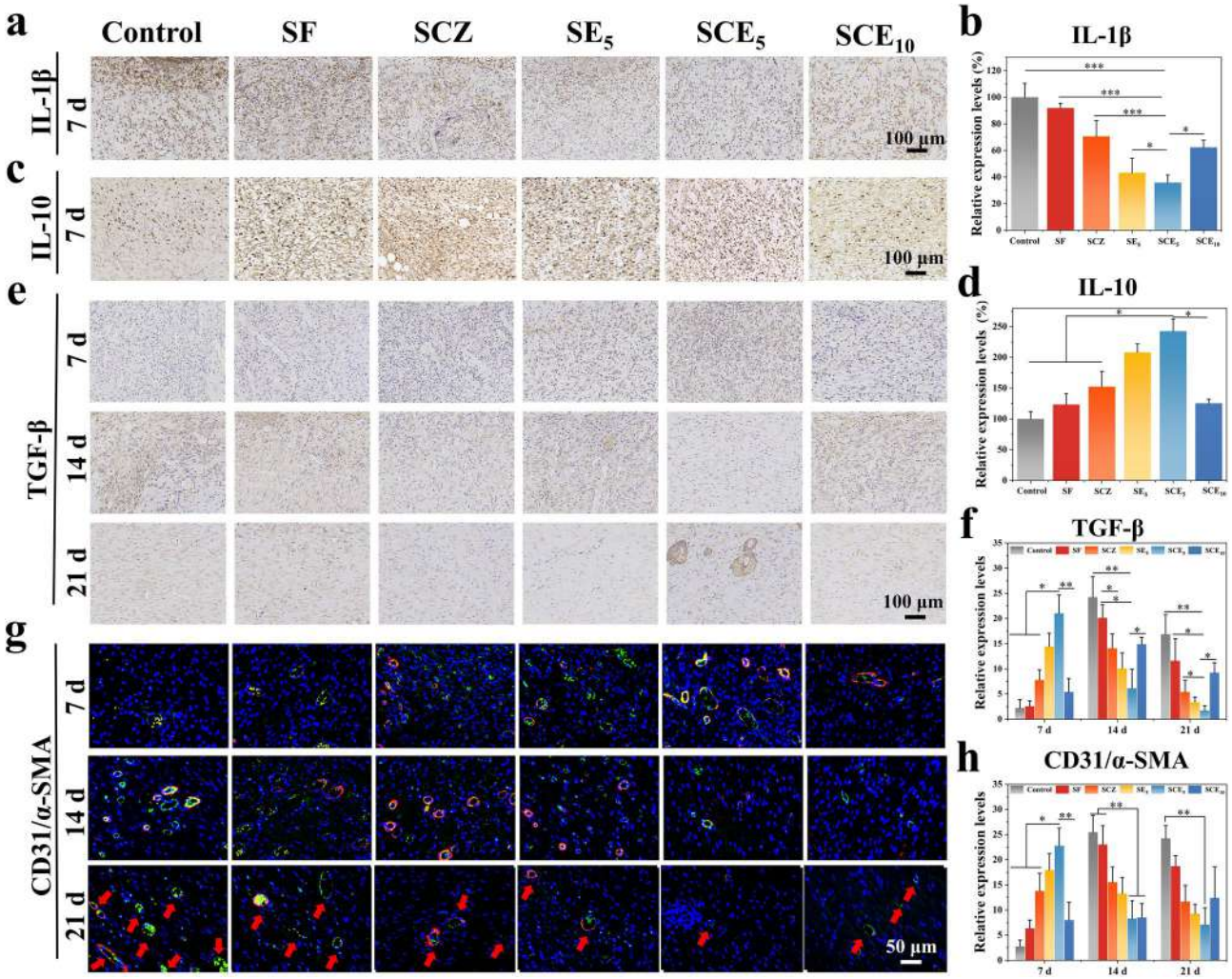

Fig. 8 Immunohistochemical and immunofluorescence staining results. **a** Representative IL-1β immunohistochemical staining images and **b** relative expression levels of IL-1β ($n=5$). **c** Representative IL-10 immunohistochemical staining images and **d** relative expression levels of IL-10 on day 7 ($n=5$). **e** Representative TGF-β immunohistochemical staining images and **f** their relative expression levels of TGF-β on days 7, 14, and 21 ($n=5$). **g** CD31 (green)/α-SMA (red) immunofluorescence colocalization staining images and **h** their relative expression levels on days 7, 14, and 21 ($n=5$). $^{*}p<0.05$, $^{**}p<0.01$, $^{***}p<0.001$

SCE_5 promotes TGF-β expression in the early stages of wound healing, enhancing wound healing, while reducing its expression in later stages to minimize scar formation.

Angiogenesis during the inflammation and proliferation phases is crucial for ensuring the delivery of nutrients and oxygen to the wound site, maintaining fibroblast proliferation, and promoting collagen synthesis and re-epithelialization. However, uncontrolled angiogenesis can stimulate scar formation and promote pathological processes such as fibrosis, tumor progression, and various hyperproliferative diseases [38]. CD31 is highly expressed in endothelial cells and is commonly used to identify newly formed blood vessels. α-SMA, a typical actin isoform in smooth muscle cells, is often used as a marker for newly formed blood vessels. Therefore, vascular formation during wound healing was evaluated using immunofluorescence for the detection of CD31/α-SMA. As shown in Fig. 8 g and h, the SCE_5 group possessed the highest expression levels of CD31/α-SMA on day 7 (22.76 ± 3.51%), and the expression levels of CD31/α-SMA gradually decreased for the SE_5, SCZ, SF and control groups, with the control group presenting levels of (2.76 ± 1.23)%, which was consistent with the natural wound healing process. However, on day 14, due to the extensive release of EGCG, angiogenesis was inhibited for the SE_5, SCE_5, and SCE_{10} groups, with the expression levels of CD31/α-SMA being decreasing to (13.26 ± 3.22)%, (8.29 ± 3.59)%, (8.52 ± 2.72)%, respectively. Whereas, for the control, SF, and SCZ groups without EGCG, new blood vessel formation was not obviously suppressed as the natural wound healing process progressed. By day 21, near-complete wound healing was observed in all the groups, characterized by the

regression of non-functional vasculature, which consequently reduced the expression levels of CD31/α-SMA in all experimental groups. Notably, the SCE_5 group exhibited the lowest expression levels of CD31/α-SMA of (7.08 ± 3.34)%. Combining the degree of vascularization in the final healed skin tissue and collagen deposition, the SCE_5 group showed the lightest degree of vascularization and the best outcome in terms of skin tissue regeneration. SCE_5 effectively inhibited pathological angiogenesis and subsequent scar formation through an EGCG-mediated mechanism. As the most abundant natural bioactive component in tea, EGCG demonstrates not only excellent biocompatibility, but also unique multi-target regulatory capacities during wound healing [61]. Studies have shown that this polyphenolic compound possesses diverse biological activities including antioxidant/free radical scavenging, anti-inflammatory, and antimicrobial properties, all of which collectively facilitate cutaneous wound healing [62]. Importantly, in the appropriate concentration range, EGCG induces dose-dependent G1-phase cell cycle arrest in vascular endothelial cells without compromising cell viability, thereby significantly inhibiting their proliferative potential [63]. Moreover, the underlying molecular mechanism of angiogenesis inhibition involves the suppression of extracellular regulated protein kinases (ERK) and protein kinase B (Akt) phosphorylation, leading to inhibition of the HIF-1α-VEGF regulatory axis and the consequent downregulation of VEGF expression [64, 65]. Although current widely used anti-angiogenic drugs, such as bevacizumab and ranibizumab, also target VEGF inhibition, they are limited by high treatment cost, potential adverse effects (e.g., wound healing complications, systemic toxicity, etc.), and easy to develop drug resistance in long-term use [66]. Histological analysis reveals no significant differences or abnormal pathological alterations in the major organs (heart, liver, spleen, lung, and kidney) of SCE-treated rats compared with those of the control rats (Fig. S12), preliminarily suggesting that the SCE dressing did not induce noticeable histopathological toxicity. Therefore, the SCE_5 dressing incorporating EGCG sustained-release technology has significant clinical advantages and broad prospects for application in promoting scarless wound healing.

2.10 Surface Microecology of Healed Skin Tissue Under SCE Intervention

In recent years, skin microbes have been found to play important roles in protecting the host from pathogen infection, modulating host skin immunity, and maintaining skin barrier homeostasis [67–69]. A healthy skin barrier typically features a stable and diverse microbial community. Disruption of skin microbial homeostasis often indicates pathophysiological changes in the host skin, leading to various skin diseases [70, 71]. To investigate the effect of the SCE Janus adhesive dressings on the skin microbiota after wound healing, *16 s-rRNA* sequencing of the skin microbes was performed in the control and SCE groups and compared them with the original normal skin microbes of the rats (blank group) (Fig. 9). Compositional analysis at the microbial genus level revealed that the microbial community composition in the SCE group was more similar to that in the blank group. In contrast, the control group exhibited excessive colonization of *Staphylococcus*, which tends to predict a homeostatic imbalance in the prognosis of wounded skin tissue (Fig. 9a). Genus-level principal coordinate (PCOA) analysis revealed greater consistency of skin microorganisms in the SCE group after wound healing. In contrast, the microbial composition in the control group was significantly different from that in the normal skin group (Fig. 9b). The α-diversity of the three groups was further analyzed, and the results revealed that compared with the control group, the normal skin and SCE groups presented higher microbial diversity in terms of the Chao1, Faith pd, Pielou_e, Shannon, and Simpson metrics, suggesting a healthier skin microbiome composition in the SCE group after the skin tissues healed (Fig. 9c). Several studies have shown that substances such as lipids and amino acids play important physiological functions in skin homeostasis. The functional metabolic pathways of skin microorganisms were characterized by PICRUSt2 analysis, which revealed the predominant enrichment of pathways related to "amino acid biosynthesis" and "fatty acid and lipid biosynthesis ". Amino acid analogs and lipid metabolites such as fatty acid analogs appear to be actively synthesized in the SCE group, potentially playing important roles in maintaining skin barrier homeostasis (Fig. 9d). Detailed differences in the skin microbiome between the control and SCE groups were identified by linear discriminant analysis (LDA, LDA > 2, $p < 0.05$, Fig. 9e). The results revealed that *Brachybacterium* spp, the *Actinobacteria* class, and others predominated in the SCE group, whereas the control group was enriched with *Staphylococcus* spp. and *Staphylococcaceae* (Fig. 9e). Overall, the surface of the healed skin tissue after the SCE Janus adhesive dressing treatment exhibited better skin flora homeostasis, which usually predicts better quality of skin healing.

2.11 Verification of the Scar Inhibition Effect on Rabbit Ears

Delayed healing of full-thickness wounds in rabbit ears can lead to excessive and disorganized collagen deposition, vascularization, and inflammation, phenotypically similar to HS in human skin [72]. Therefore, the rabbit ear HS model was employed to study the effect of the SCE Janus adhesive dressings on scarless wound healing (Fig. 10a). New Zealand rabbits were randomly divided into three groups: (1) the untreated control group, (2) the SF group, and (3) the SCE_5 group. As shown in Fig. 10b and S13, the SCE_5

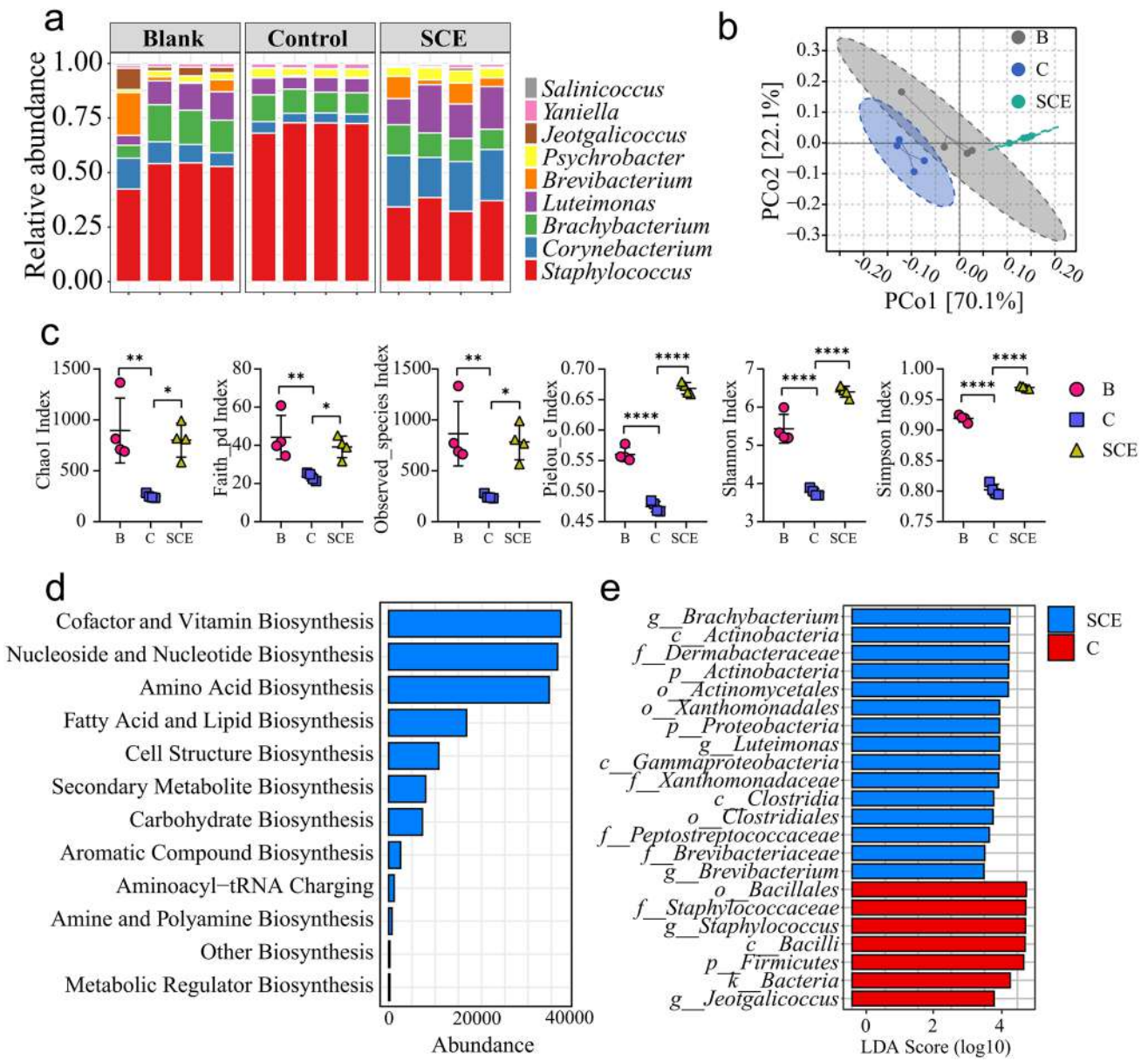

Fig. 9 Skin microbiota analysis after wound healing. **a** Skin microbiota composition at the genus level. **b** The principal coordinate analysis (PCOA) plots, and **c** α-diversity (Chao1, Faith_pd, Pielou_e, Shannon, Simpson) plots for the blank (B), control (C), and SCE_5 (SCE) groups on day 21 ($n=4$). **d** Functional prediction of the differential microbiota between SCE_5 and the control group on day 21. **e** Linear discriminant analysis (LDA) performed to compare the enriched taxa between SCE_5 (SCE) and the control (C) group. $^*p<0.05$, $^{**}p<0.01$, $^{***}p<0.001$

group exhibited near-complete epidermal re-epithelialization by day 7, resulting in a significantly higher wound closure rate ($76.76\pm5.87\%$; $p<0.001$ vs. control), while the control wounds presented impaired healing with evident exudation and bacterial colonization. By day 14, untreated wounds remained unhealed ($63.21\pm19.72\%$) with pronounced protrusion and an erythematous appearance, in stark contrast to the SCE_5-treated wounds, which presented minimal scar protrusion and near-complete healing ($95.14\pm1.58\%$). By days 21 and 28, wounds in the control group presented visible scabs, and those in the SF group showed severe local protrusions. In contrast, the wounds of the SCE_5 group were flat with visible hair growth on the surface. Moreover, the Vancouver Scar Scale (VSS) was used to assess the scars on the ears of each group of rabbits on day 28, with results presented in Fig. 10c. The control group displayed typical characteristics of HS, with deep red coloration indicating severe local vascular proliferation, fibrotic elevation, pronounced hyperplasia, and a harder texture. In contrast, the SF group showed localized surface elevations with reddish

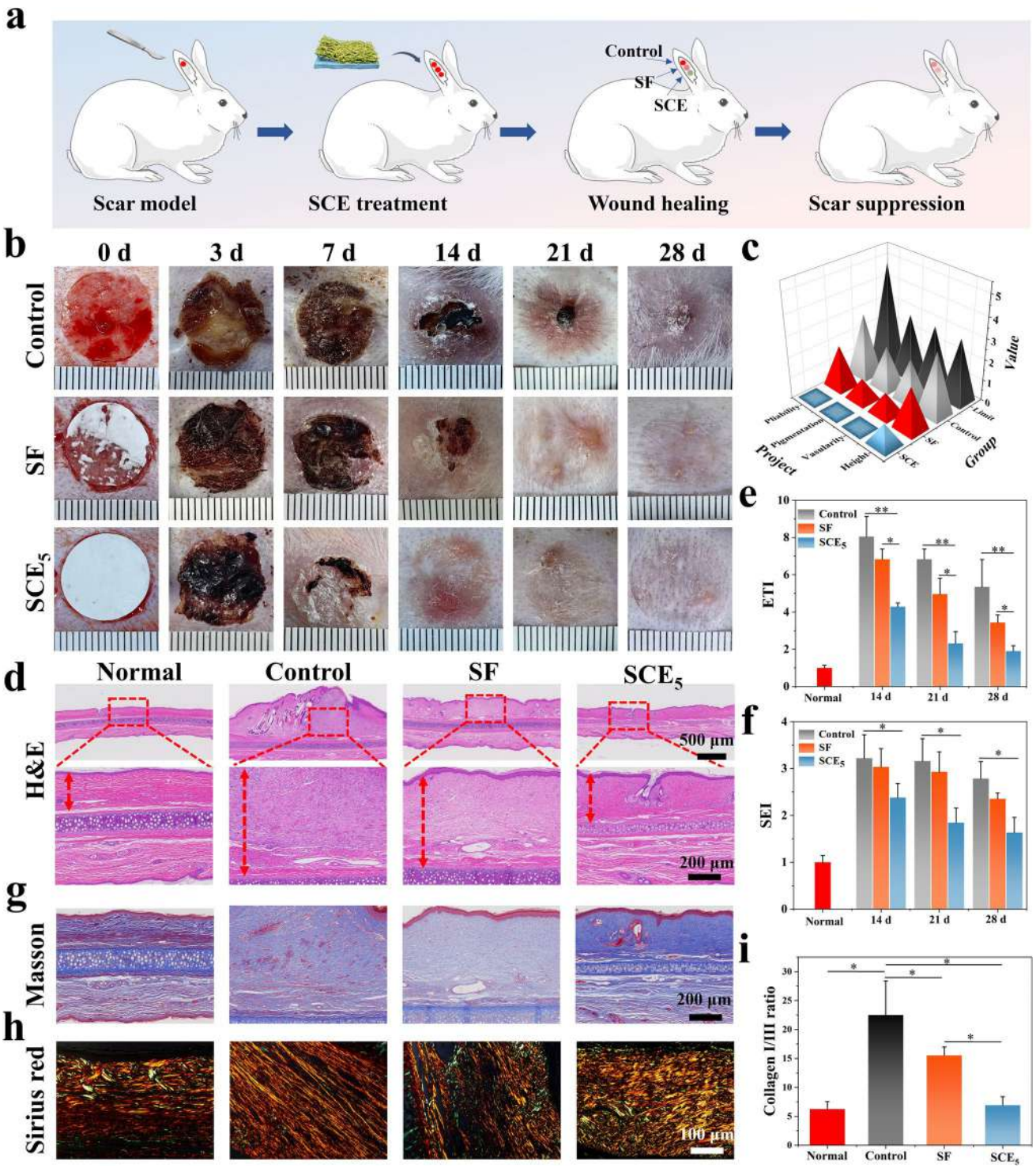

Fig. 10 In vivo evaluation in preventing rabbit ear scar formation. **a** Schematic diagram of rabbit ear scar model establishment and treatment. **b** Representative photographs of the wounds treated with different samples on days 0, 3, 7, 14, 21 and 28. **c** The rabbit ear scar scores evaluated according to the Vancouver Scar Scale (n = 6). **d** H&E staining images of rabbit ear scar tissues on day 28. **e** Epidermal thickness indices (ETI), and **f** scar elevation indices (SEI) of rabbit ear scar tissues ($n = 6$). **g** Masson's trichrome and **h** Sirius Red staining images of rabbit ear scar on day 28, and **i** the collagen type I/III ratios obtained from the Sirius Red staining images ($n = 6$). $^{*}p < 0.05$, $^{**}p < 0.01$, $^{***}p < 0.001$

discoloration at the elevated spots, while the SCE_5 group presented much smoother scar surfaces, with more blurred scar boundaries, closely resembling normal skin. These findings demonstrate that SCE_5 plays a significant role in preventing the formation of HS and in promoting skin reconstruction following wound healing.

In addition to surface morphology, the impact of each group on rabbit ear wound tissue was also examined at the histological level. The H&E staining results (Fig. 10d and S14) revealed obvious hyperplastic characteristics in the control group, including tissue elevation and chronic inflammation. Conversely, the SCE_5 group presented relatively thin epidermal and dermal collagen layers than the control group. Quantitative assessment of the epidermal thickness index (ETI) and scar elevation index (SEI) across treatment groups reveals significant improvements in the SCE_5 group by day 28 (Fig. 10e and f). The ETI and SEI values of the SCE_5-treated wounds were (1.91 ± 0.29) and (1.63 ± 0.32) respectively, showing significant reduction compared to that of the control group (ETI: 5.34 ± 1.47, $p < 0.01$; SEI: 2.75 ± 0.36, $p < 0.05$). Notably, the epidermal and dermal thickness of SCE_5-treated wounds more closely resembled those of normal rabbit ear skin (ETI: 1.00 ± 0.14 SEI: 1.00 ± 0.14). Masson's trichrome staining revealed (Fig. 10g and S14) that, compared with those in the other two groups, the arrangement of collagen fibers in the healed skin after SCE_5 treatment was more orderly and aligned. The ratio of type I/type III collagen was further analyzed using Sirius Red staining to observe the degree of collagen deposition after tissue healing (Fig. 10 h, i and S15). The results show that in normal skin and HS tissue in the control group, the ratios of type I (red)/type III (green) collagen were (6.25 ± 1.27) and (22.50 ± 5.88) (Fig. 10i), respectively. In contrast, after SCE_5 treatment, the ratio of collagen I/III in the healed skin sharply decreased to (6.92 ± 1.44), closer to those of normal rabbit ears and significantly different from those of the control group ($p < 0.05$). These findings indicate that SCE_5 treatment effectively inhibited the excessive deposition of type I collagen and promoted the formation of type III collagen, as type I collagen is usually considered a prominent component of HS. Meanwhile, as shown in Fig. S16, analysis of collagen fiber alignment angles in Sirius Red-stained sections using ImageJ software revealed that the collagen fiber orientation in SCE-treated wound areas more closely resembled that in normal skin. This finding is consistent with the established histological characteristics of skin tissue: collagen fibers in the normal dermis exhibit a random basket-weave pattern (with wide angular distribution), whereas scar tissue typically shows unidirectional parallel alignment of collagen bundles (with highly consistent orientation angles, predominantly parallel to the epidermal surface) [73]. Current clinically prevalent scar-inhibiting dressings primarily include silicone gel sheets, hydrocolloids and among others [74]. Silicone gel sheets act through multiple mechanisms, including the creation of an occlusive barrier to minimize water evaporation and maintain wound hydration, the exertion of mechanical compression through tissue adhesion, and the release of silicone oils that penetrate the stratum corneum to chemically modulate scar formation [75]. Conversely, hydrocolloid dressings operate principally by establishing a moist wound environment that suppresses bacterial infection and inflammatory responses, thereby facilitating accelerated wound healing and reduced scar hyperplasia [76]. SCE dressings synergistically combine the predominant advantages of both dressing types, demonstrating a unique capacity for temporally regulating wound healing progression while crucially targeting pathological angiogenesis during later healing stages to fundamentally disrupt scar formation pathways, ultimately leading to optimal scarless wound healing.

2.12 Temporal Characteristics of the Transcriptome of Wound Healing Tissues under SCE Intervention

To comprehensively assess the effects of the SCE Janus adhesive dressings intervention on wound healing at different stages, rabbit ear skin tissues were collected on days 14, 21, and 28 of the healing process for transcriptome sequencing ($n = 3$). As shown in Fig. 11a, the results of the gene clustering analysis showed that the rabbit ear tissues treated with the SCE Janus adhesive dressings were characteristically different from those in the control group at different time points, especially on day 28. Furthermore, the normal rabbit ear skin tissues were sequenced to determine gene expression in these rabbit ear skin tissues. Interestingly, the SCE Janus adhesive dressings-treated rabbit ear wound tissues showed greater transcriptome profile similarity to normal skin tissues by day 28 post-trauma, whereas they were significantly different from those in the control group (Fig. 11b). With respect to the KEGG pathways, the three stages of wound healing showed enrichment of pathways closely related to wound healing and scar formation, such as "cell adhesion molecules", "Wnt signaling pathway", "ECM–receptor interaction", and "focal adhesion" (Fig. S17-19). To further understand the role of the SCE Janus adhesive dressings in the microenvironment of rabbit ear skin wounds, a GO enrichment analysis was performed. The up-regulated and down-regulated functional pathways in rabbit ear skin tissues were analyzed from the inflammation, proliferation, and remodeling phases of the wound, respectively. In addition, the expression of key genes at different stages of rabbit ear wound healing was examined under the SCE Janus adhesive dressing intervention. Based on the gene expression results, representative cytokines were selected for immunohistochemical validation.

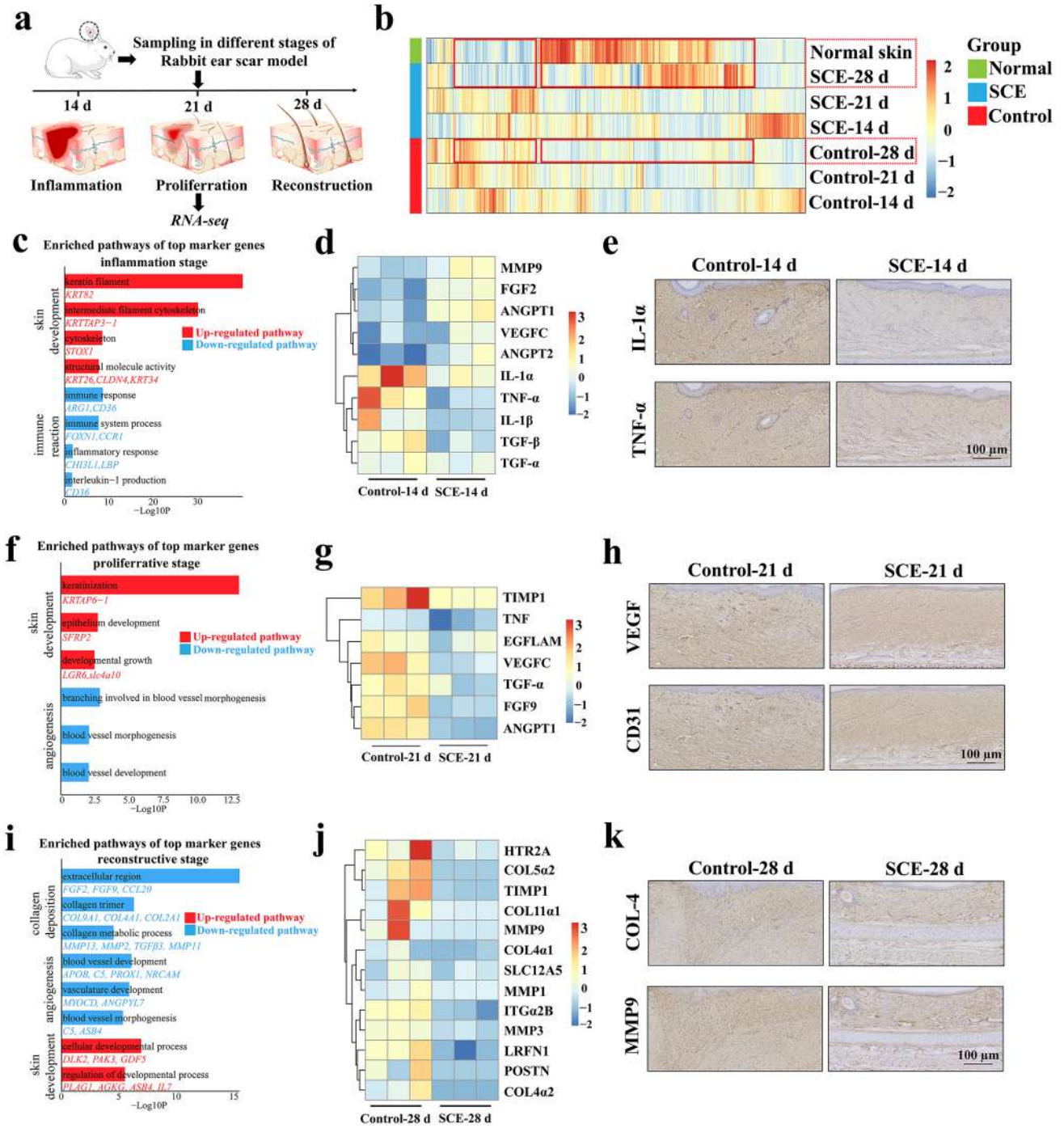

Fig. 11 Transcriptome sequencing and immunohistochemical staining images of rabbit ear wound scar tissues. **a** Schematic diagram of sampling for transcriptome sequencing. **b** Transcriptome gene expression heatmaps in control, SCE, and normal skin tissues. **c** Transcriptome GO pathway analysis results. **d** Heatmap for inflammation-related genes. **e** IL-1α and TNF-α immunohistochemical staining images of rabbit ear skin tissues on day 14. **f** Transcriptome GO pathway analysis. **g** Heatmap of angiogenesis-related genes. **h** CD31 and VEGF immunohistochemical staining images of rabbit ear skin tissues on day 21. **i** Transcriptome GO pathway analysis. **j** Enlarged heatmap of collagen formation-related genes. **k** COL-4 and MMP9 immunohistochemical staining images of rabbit ear skin tissues on day 28

During the inflammation phase of the wound, the "skin development" pathway, which is often a positive sign of wound epithelialization, was significantly up-regulated in the SCE group compared with the control group on day 14. In contrast, inflammation-related pathways such as the "immune response", "inflammatory response", "interleukin-1

production" and other functional pathways closely related to inflammation were down-regulated in the SCE group. These findings suggest a significant anti-inflammatory effect of the SCE Janus adhesive dressings compared with the control (Fig. 11c). Notably, the SCE group demonstrated significantly lower expression levels of key inflammation-related genes (including IL-1α, TNF-α, and IL-1β) than the control group (Fig. 11d). These findings were further corroborated by the immunohistochemical staining of rabbit ear wounds. The quantitative analysis results (Fig. 11e and S20) also revealed that the IL-1α (31.76 ± 6.06%) and TNF-α (45.83 ± 6.40%) expression levels of the SCE group were all significantly lower ($p < 0.001$) than the control group (set as 100%).

As the wound progressed to the proliferation phase, the SCE group significantly promoted the development, proliferation, and differentiation of rabbit ear skin tissues, as shown in Fig. 11f. The functional pathways of "keratinization", "epidermal cell differentiation", "skin development", and "epidermal development" were significantly enriched during this period. The proliferation phase represents a critical stage for neovascularization in wound healing. Application of SCE Janus adhesive dressings significantly inhibited neovascularization, as evidenced by GO pathway analysis showing downregulation of "vasculogenesis" and "angiopoietin" signaling pathways (Fig. 11f). Notably, the SCE group demonstrated significantly lower expression of the key angiogenic regulators (TIMP1, VEGFC, ANGPT1, etc., Fig. 11g). Quantitative immunohistochemical analysis further revealed markedly lower expression of VEGF (52.17 ± 12.03%, $p < 0.01$) and CD31 (47.47 ± 6.33%, $p < 0.001$) in the SCE-treated wounds compared to the control group (Fig. 11h and S21). Collectively, these findings indicate that the SCE dressing can precisely modulate angiogenesis dynamics during wound healing. As the wound heals, the final stage of remodeling begins with collagen deposition and degradation, after re-epithelialization of the wound is completed. As shown in Fig. 11i, the expression of collagen deposition-related components, such as extracellular matrix components and collagen metabolism factors, was down-regulated in the SCE group compared with the control group, we found that in SCE vs control, the expression of collagen deposition components such as extracellular matrix components and collagen metabolism was down-regulated in the SCE group. The neovascularization component of the SCE Janus adhesive dressings, represented by "tube development", "tube formation" and "vascularization", was also down-regulated. This finding suggests that the inhibitory effect of the SCE Janus adhesive dressings on vascularization continues until the final stage of wound healing and is closely related to the reduced scarring of the skin wounds in rabbit ears treated. Moreover, as shown in Fig. 11j, the SCE group showed low expression of genes related to collagen production, such as COL5α2, COL4α1, and COL4α2, in comparison with the control group. *Postn* has been found to be the key gene responsible for the difference between normal skin and keloid tissue, and *Postn* also demonstrated low expression in the SCE group. Notably, matrix metalloproteinase (MMP), particularly MMP9, which are associated with angiogenesis, were still highly expressed in the control group, suggesting that abnormal angiogenic activity still existed in the control group at this healing stage, whereas these two genes appeared suppressed in the SCE group. Then, COL-4 and MMP9 were subsequently selected for verification in rabbit ear tissue (Fig. 11k), and the results were consistent with those shown in Fig. 11j. Quantitative immunohistochemical analysis further revealed markedly lower expression of COL-4 (67.65 ± 10.35% of the control group, $p < 0.05$) and MMP9 (54.68 ± 6.54% of the control group, $p < 0.01$) in SCE-treated wounds than in control wounds (Fig. S22). In summary, the temporal characteristics of the transcriptome of rabbit skin tissues during wound healing under the SCE Janus adhesive dressing intervention included a decreased inflammatory response in the inflammation phase, inhibition of angiogenesis in the proliferation phase, and limited collagen synthesis in the remodeling phase.

Given the excellent performance of the SCE Janus adhesive dressings in scarless wound healing both in vitro and in vivo, these dressings demonstrated significant potential for clinical applications. However, the clinical translation of SCE dressings still needs to address four major challenges. Firstly, a self-designed large-scale electrospinning equipment is needed for the batch preparation of core–shell nanofibers. Alternative strategies such as coaxial wet spinning could be considered to replace electrospinning, in order to support large-scale production of core–shell micro-/nanofibers. Secondly, long-term stability testing and accelerated aging experiments should be conducted to determine the shelf-life of SCE Janus adhesive dressings, and necessary formulation adjustments might be needed to confer the dressing with a reasonable shelf-life in the range of 1–3 years. Additionally, although rat full-thickness skin wound and rabbit ear scar models have demonstrated their potential for scarless wound healing, standardized clinical trials are required to evaluate its safety and efficacy, along with establishing a complete risk control system to meet regulatory requirements. Finally, the classification and definition of medical devices by the National Medical Products Administration (NMPA) of China for the adhesive dressing is needed before its registration license application, as it contains EGCG. If the dressing is defined not as a medical device, but as a drug–device combination product, its clinical translation needs a longer period. Addressing these translational challenges is critical to translating this product from the laboratory to the clinic.

3 Conclusions

In this study, the SCE Janus adhesive dressings are developed to target post-traumatic scarring, a key clinical challenge. The hydrophilic upper layer of this dressing is mainly composed of silk electrospun fibers with an EGCG core, and the hydrophobic lower layer is composed of silk electrospun film modified with Ca^{2+}/Zn^{2+}. Furthermore, the SCE Janus adhesive dressings are characterized by their adhesiveness, degradability, and biocompatibility. More importantly, they serve as a biological timer that regulates wound healing and prevents excessive post-traumatic scarring. Specifically, the SCE Janus adhesive dressings exert their pro-healing and scarless healing effects through anti-inflammatory effects during the inflammation phase of the wound, inhibition of excessive angiogenesis in the wound bed during the proliferation phase, and limitation of excessive collagen deposition leading to scar formation during the remodeling phase. In the rat wound model, the SCE Janus adhesive dressings rapidly promoted wound healing. In the rabbit ear scarring model, the SCE Janus adhesive dressings significantly reduced scarring by exerting effects during different stages of wound healing. RNA-seq analysis of rabbit ear tissues showed that the SCE Janus adhesive dressings exerted their effects mainly by inhibiting inflammation in the inflammation stage, inhibiting angiogenesis in the proliferation phase, and modulating collagen deposition in the remodeling stage. In conclusion, the SCE Janus adhesive dressings have potential for a wide range of therapeutic applications, including the treatment of skin wounds and the prevention of scar formation.

Supplementary Information The online version contains supplementary material available at https://doi.org/10.1007/s42765-025-00620-y.

Acknowledgements This work was financially by the Natural Science Foundation of China (Grant Nos. 82272453, U21A2099 and 82472133), the Guangdong Basic and Applied Basic Research Foundation (Grant Nos. 2024A1515012664), and the Shenzhen Medical Research Special Fund (Grant No. A2402019).

Authors' Contributions Meimei Fu: conceptualization, methodology and investigation, software and validation, formal analysis, funding acquisition, writing—original draft. Yue Li: methodology and investigation, software and validation, formal analysis, writing—review and editing. Yitao Zhao: methodology and investigation, visualization, software, writing—review and editing. Yuting Zhu: methodology, formal analysis, visualization. Zhou Fang: methodology, formal analysis, visualization. Zhuoyi Huang: data curation, software. Wenjun Luo: methodology and investigation, software. Xinyu Huang: conceptualization, methodology and investigation. Jintao Li: conceptualization, supervision and project administration. Zhiqi Hu: conceptualization, supervision and project administration, funding acquisition. Keke Wu: conceptualization, supervision and project administration, funding acquisition, writing—review and editing. Jinshan Guo: conceptualization, supervision and project administration, funding acquisition, writing—review and editing.

Funding The Natural Science Foundation of China, 82272453, Jinshan Guo, U21A2099, Jinshan Guo; 82472133, Keke Wu, the Guangdong Basic and Applied Basic Research Foundation, 2024A1515012664, Jinshan Guo, the Shenzhen Medical Research Special Fund, A2402019, Zhiqi Hu.

Data Availability The data that support the findings of this study are available from the corresponding author upon reasonable request.

Declarations

Conflict of Interest The authors declare that they have no conflict of interest.

References

1. Henderson NC, Rieder F, Wynn TA. Fibrosis: from mechanisms to medicines. *Nature* **2020**;*587*:555.
2. Moretti L, Stalfort J, Barker TH, Abebayehu D. The interplay of fibroblasts, the extracellular matrix, and inflammation in scar formation. *J Biol Chem*. **2022**;*298*: 101530.
3. Keane TJ, Horejs CM, Stevens MM. Scarring vs. functional healing: matrix-based strategies to regulate tissue repair. *Adv Drug Deliv Rev*. **2018**;*129*:407.
4. Finnerty CC, Jeschke MG, Branski LK, Barret JP, Dziewulski P, Herndon DN. Hypertrophic scarring: the greatest unmet challenge after burn injury. *Lancet* **2016**;*388*:1427.
5. Rodrigues M, Kosaric N, Bonham CA, Gurtner GC. Wound healing: a cellular perspective. *Physiol Rev*. **2019**;*99*:665.
6. Zhang J, Zheng Y, Lee J, Hua J, Li S, Panchamukhi A, Yue J, Gou X, Xia Z, Zhu L, Wu X. A pulsatile release platform based on photo-induced imine-crosslinking hydrogel promotes scarless wound healing. *Nat Commun*. **2021**;*12*:1670.
7. Deng F, Yang R, Yang Y, Li X, Hou J, Liu Y, Lu J, Huangfu S, Meng Y, Wu S, Zhang L. Visible light accelerates skin wound healing and alleviates scar formation in mice by adjusting STAT3 signaling. *Commun Biol*. **2024**;*7*:1266.
8. Wu M, Zhao Y, Tao M, Fu M, Wang Y, Liu Q, Lu Z, Guo J. Malate-based biodegradable scaffolds activate cellular energetic metabolism for accelerated wound healing. *ACS Appl Mater Interfaces* **2023**;*15*:50836.
9. Jeschke MG, Wood FM, Middelkoop E, Bayat A, Teot L, Ogawa R, Gauglitz GG. Scars. *Nat Rev Dis Primers* **2023**;*9*:64.
10. Mbituyimana B, Bukatuka CF, Qi F, Ma G, Shi Z, Yang G. Microneedle-mediated drug delivery for scar prevention and treatment. *Drug Discov Today* **2023**;*28*: 103801.
11. Jonidi Shariatzadeh F, Currie S, Logsetty S, Spiwak R, Liu S. Enhancing wound healing and minimizing scarring: a comprehensive review of nanofiber technology in wound dressings. *Prog Mater Sci*. **2025**;*147*: 101350.
12. Cao X, Wu X, Zhang Y, Qian X, Sun W, Zhao Y. Emerging biomedical technologies for scarless wound healing. *Bioact Mater*. **2024**;*42*:449.
13. Coentro JQ, Pugliese E, Hanley G, Raghunath M, Zeugolis DI. Current and upcoming therapies to modulate skin scarring and fibrosis. *Adv Drug Deliv Rev*. **2019**;*146*:37.
14. An R, Shi C, Tang Y, Cui Z, Li Y, Chen Z, Xiao M, Xu L. Chitosan/rutin multifunctional hydrogel with tunable adhesion, anti-inflammatory and antibacterial properties for skin wound healing. *Carbohydr Polym*. **2024**;*343*: 122492.
15. Liu T. Recent advances in reactive oxygen species scavenging nanomaterials for wound healing. *Exploration* **2024**;*4*:20230066.

16. Yi Y, Yang Z, Zhou C, Yang Y, Wu Y, Zhang Q. Quercetin-encapsulated GelMa hydrogel microneedle reduces oxidative stress and facilitates wound healing. *Nano TransMed*. **2024**;*3*: 100030.
17. Liu L, Ding Z, Yang Y, Zhang Z, Lu Q, Kaplan DL. Asiaticoside-laden silk nanofiber hydrogels to regulate inflammation and angiogenesis for scarless skin regeneration. *Biomater Sci*. **2021**;*9*:5227.
18. Hong Y, Wang M, Hu D, Wang Y, Ji S, Xiang J, Zhang H, Chen H, Li Y, Xiong M, Pi W, Wang Q, Yang X, Li Y, Shui C, Wang X, Fu X, Sun X. NIR-responsive multifunctional artificial skin for regenerative wound healing. *Adv Funct Mater*. **2024**;*34*: 2405876.
19. Rybak D, Du J, Nakielski P, Rinoldi C, Kosik-Kozioł A, Zakrzewska A, Wu H, Li J, Li X, Yu Y, Ding B, Pierini F. Nir-light activable 3D printed platform nanoarchitectured with electrospun plasmonic filaments for on demand treatment of infected wounds. *Adv Healthc Mater*. **2025**;*14*: 2404274.
20. Qi X, Li Y, Xiang Y, Chen Y, Shi Y, Ge X, Zeng B, Shen J. Hyperthermia-enhanced immunoregulation hydrogel for oxygenation and ROS neutralization in diabetic foot ulcers. *Cell Biomater*. **2025**;*1*: 100020.
21. Zhang Y, Wang S, Yang Y, Zhao S, You J, Wang J, Cai J, Wang H, Wang J, Zhang W, Yu J, Han C, Zhang Y, Gu Z. Scarless wound healing programmed by core-shell microneedles. *Nat Commun*. **2023**;*14*:3431.
22. Yang Y, Suo D, Xu T, Zhao S, Xu X, Bei HP, Wong KK, Li Q, Zheng Z, Li B, Zhao X. Sprayable biomimetic double mask with rapid autophasing and hierarchical programming for scarless wound healing. *Sci Adv*. **2024**;*10*: eado9479.
23. Liu X, Sun Y, Wang J, Kang Y, Wang Z, Cao W, Ye J, Gao C. A tough, antibacterial and antioxidant hydrogel dressing accelerates wound healing and suppresses hypertrophic scar formation in infected wounds. *Bioact Mater*. **2024**;*34*:269.
24. Xu N, Yuan Y, Ding L, Li J, Jia J, Li Z, He D, Yu Y. Multifunctional chitosan/gelatin@tannic acid cryogels decorated with in situ reduced silver nanoparticles for wound healing. *Burns Trauma* **2022**;*10*: tkac019.
25. Guo Y, Huang J, Fang Y, Huang H, Wu J. 1D, 2D, and 3D scaffolds promoting angiogenesis for enhanced wound healing. *Chem Eng J*. **2022**;*437*: 134690.
26. Wang X, Li R, Zhao H. Enhancing angiogenesis: Innovative drug delivery systems to facilitate diabetic wound healing. *Biomed Pharmacother*. **2024**;*170*: 116035.
27. Olgasi C, Assanelli S, Cucci A, Follenzi A. Hemostasis and endothelial functionality: the double face of coagulation factors. *Haematologica* **2024**;*109*:2041.
28. Yu Y, Dai K, Gao Z, Tang W, Shen T, Yuan Y, Wang J, Liu C. Sulfated polysaccharide directs therapeutic angiogenesis via endogenous tgftg secretion of macrophages. *Sci Adv*. **2021**;*7*: eabd8217.
29. Yang P, Lu Y, Gou W, Qin Y, Zhang X, Li J, Zhang Q, Zhang X, He D, Wang Y, Xue D, Liu M, Chen Y, Zhou J, Zhang X, Lv J, Tan J, Luo G, Zhang Q. *Andrias davidianus* derived glycosaminoglycans direct diabetic wound repair by reprogramming reparative macrophage glucolipid metabolism. *Adv Mater*. **2025**;*37*: 2417801.
30. Liu H, Qin S, Zhang H, Chen Z, Zhao Y, Liu J, Deng Y, Liu M, Chen W, Wang Z, Wang L. Silk Sericin-based ROS-responsive oxygen generating microneedle platform promotes angiogenesis and decreases inflammation for scarless diabetic wound healing. *Adv Funct Mater*. **2025**;*35*:2404461.
31. Fu M, Zhao Y, Wang Y, Li Y, Wu M, Liu Q, Hou Z, Lu Z, Wu K, Guo J. On-demand removable self-healing and pH-responsive europium-releasing adhesive dressing enables inflammatory microenvironment modulation and angiogenesis for diabetic wound healing. *Small* **2023**;*19*: e2205489.
32. Shao Z, Yin T, Jiang J, He Y, Xiang T, Zhou S. Wound microenvironment self-adaptive hydrogel with efficient angiogenesis for promoting diabetic wound healing. *Bioact Mater*. **2023**;*20*:561.
33. Fu YJ, Shi YF, Wang LY, Zhao YF, Wang RK, Li K, Zhang ST, Zha XJ, Wang W, Zhao X, Yang W. All-natural immunomodulatory bioadhesive hydrogel promotes angiogenesis and diabetic wound healing by regulating macrophage heterogeneity. *Adv Sci*. **2023**;*10*: 2206771.
34. Shen Y, Xu G, Huang H, Wang K, Wang H, Lang M, Gao H, Zhao S. Sequential release of small extracellular vesicles from bilayered thiolated alginate/polyethylene glycol diacrylate hydrogels for scarless wound healing. *ACS Nano* **2021**;*15*:6352.
35. Wu K, Fu M, Zhao Y, Gerhard E, Li Y, Yang J, Guo J. Antioxidant anti-inflammatory and antibacterial tannin-crosslinked citrate-based mussel-inspired bioadhesives facilitate scarless wound healing. *Bioact Mater*. **2023**;*20*:93.
36. Yuan B, Upton Z, Leavesley D, Fan C, Wang XQ. Vascular and collagen target: a rational approach to hypertrophic scar management. *Adv Wound Care* **2021**;*12*:38.
37. Boucher JM, Clark RP, Chong DC, Citrin KM, Wylie LA, Bautch VL. Dynamic alterations in decoy VEGF receptor-1 stability regulate angiogenesis. *Nat Commun*. **2017**;*8*:15699.
38. Korntner S, Lehner C, Gehwolf R, Wagner A, Grütz M, Kunkel N, Tempfer H, Traweger A. Limiting angiogenesis to modulate scar formation. *Adv Drug Deliv Rev*. **2019**;*146*:170.
39. Wu Y, Zhang Q, Ann DK, Akhondzadeh A, Duong HS, Messadi DV, Le AD. Increased vascular endothelial growth factor may account for elevated level of plasminogen activator inhibitor-1 via activating ERK1/2 in keloid fibroblasts. *Am J Physiol Cell Physiol*. **2004**;*286*:C905.
40. Aarabi S, Longaker MT, Gurtner GC. Hypertrophic scar formation following burns and trauma: new approaches to treatment. *PLoS Med*. **2007**;*4*: e234.
41. Gira AK, Brown LF, Washington CV, Cohen C, Arbiser JL. Keloids demonstrate high-level epidermal expression of vascular endothelial growth factor. *J Am Acad Dermatol*. **2004**;*50*:850.
42. Han C, Barakat M, DiPietro LA. Angiogenesis in wound repair: too much of a good thing? *Cold Spring Harb Perspect Biol*. **2022**;*14*: a041225.
43. Tran HA, Hoang TT, Maraldo A, Do TN, Kaplan DL, Lim KS, Rnjak-Kovacina J. Emerging silk fibroin materials and their applications: new functionality arising from innovations in silk crosslinking. *Mater Today* **2023**;*65*:244.
44. Reizabal A, Costa CM, Pérez-Álvarez L, Vilas-Vilela JL, Lanceros-Méndez S. Silk fibroin as sustainable advanced material: material properties and characteristics, processing, and applications. *Adv Funct Mater*. **2023**;*33*: 2210764.
45. Forouzideh N, Nadri S, Fattahi A, Abdolahinia ED, Habibizadeh M, Rostamizadeh K, Baradaran-Rafii A, Bakhshandeh H. Epigallocatechin gallate loaded electrospun silk fibroin scaffold with anti-angiogenic properties for corneal tissue engineering. *J Imaging Sci Technol*. **2020**;*56*: 101498.
46. Tsakiroglou P, VandenAkker NE, Del Bo C, Riso P, Klimis-Zacas D. Role of berry anthocyanins and phenolic acids on cell migration and angiogenesis: an updated overview. *Nutrients* **2019**;*11*:1075.
47. Alizadeh S, Samadikuchaksaraei A, Jafari D, Orive G, Dolatshahi-Pirouz A, Pezeshki-Modaress M, Gholipourmalekabadi M. Enhancing diabetic wound healing through improved angiogenesis: the role of emulsion-based core-shell micro/nanofibrous scaffold with sustained CuO nanoparticle delivery. *Small* **2024**;*20*: e2309164.
48. Bi S, Lin H, Zhu K, Zhu Z, Zhang W, Yang X, Chen S, Zhao J, Liu M, Pan P, Liang G. Chitosan-salvianolic acid B coating on the surface of nickel-titanium alloy inhibits proliferation of smooth

muscle cells and promote endothelialization. *Front Bioeng Biotechnol*. **2023**;*11*:1300336.
49. Amini Moghaddam M, Di Martino A, Šopík T, Fei H, Císař J, Pummerová M, Sedlařík V. Polylactide/Polyvinylalcohol-based porous bioscaffold loaded with gentamicin for wound dressing applications. *Polymers* **2021**;*13*: 921.
50. Seo JW, Kim H, Kim K, Choi SQ, Lee HJ. Calcium-modified silk as a biocompatible and strong adhesive for epidermal electronics. *Adv Funct Mater*. **2018**;*28*:1800802.
51. Liu Z, Tang W, Liu J, Han Y, Yan Q, Dong Y, Liu X, Yang D, Ma G, Cao H. A novel sprayable thermosensitive hydrogel coupled with zinc modified metformin promotes the healing of skin wound. *Bioact Mater*. **2023**;*20*:610.
52. Subramaniam T, Fauzi MB, Lokanathan Y, Law JX. The role of calcium in wound healing. *Int J Mol Sci*. **2021**;*22*: 6486.
53. Lei Q, He D, Ding L, Kong F, He P, Huang J, Guo J, Brinker CJ, Luo G, Zhu W, Yu Y. Microneedle patches integrated with biomineralized melanin nanoparticles for simultaneous skin tumor photothermal therapy and wound healing. *Adv Funct Mater*. **2022**;*32*: 2113269.
54. Xu N, Gao Y, Li Z, Chen Y, Liu M, Jia J, Zeng R, Luo G, Li J, Yu Y. Immunoregulatory hydrogel decorated with tannic acid/ferric ion accelerates diabetic wound healing via regulating macrophage polarization. *Chem Eng J*. **2023**;*466*: 143173.
55. Qian Y, Ding J, Zhao R, Song Y, Yoo J, Moon H, Koo S, Kim JS, Shen J. Intrinsic immunomodulatory hydrogels for chronic inflammation. *Chem Soc Rev*. **2025**;*54*:33.
56. Tonnesen MG, Feng X, Clark RAF. Angiogenesis in wound healing. *J Invest Dermatol Symp Proc*. **2000**;*5*:40.
57. Tao B, Lin C, Guo A, Yu Y, Qin X, Li K, Tian H, Yi W, Lei D, Chen L. Fabrication of copper ions-substituted hydroxyapatite/polydopamine nanocomposites with high antibacterial and angiogenesis effects for promoting infected wound healing. *Ind Eng Chem*. **2021**;*104*:345.
58. Bhol NK, Bhanjadeo MM, Singh AK, Dash UC, Ojha RR, Majhi S, Duttaroy AK, Jena AB. The interplay between cytokines, inflammation, and antioxidants: mechanistic insights and therapeutic potentials of various antioxidants and anti-cytokine compounds. *Biomed Pharmacother*. **2024**;*178*: 117177.
59. Yaseen MM, Abuharfeil NM, Darmani H, Daoud A. Mechanisms of immune suppression by myeloid-derived suppressor cells: the role of interleukin-10 as a key immunoregulatory cytokine. *Open Biol*. **2020**;*10*: 200111.
60. Shi A, Li J, Qiu X, Sabbah M, Boroumand S, Huang TC, Zhao C, Terzic A, Behfar A, Moran SL. TGF-β loaded exosome enhances ischemic wound healing in vitro and in vivo. *Theranostics* **2021**;*11*:6616.
61. Li Q, Song H, Li S, Hu P, Zhang C, Zhang J, Feng Z, Kong D, Wang W, Huang P. Macrophage metabolism reprogramming EGCG-Cu coordination capsules delivered in polyzwitterionic hydrogel for burn wound healing and regeneration. *Bioact Mater*. **2023**;*29*:251.
62. Gu Y, You Y, Yang Y, Liu X, Yang L, Li Y, Zhang C, Yang H, Sha Z, Ma Y, Pang Y, Liu Y. Multifunctional EGCG@ZIF-8 nanoplatform with photodynamic therapy/chemodynamic therapy antibacterial properties promotes infected wound healing. *ACS Appl Mater Interfaces* **2024**;*16*:50238.
63. Kciuk M, Alam M, Ali N, Rashid S, Głowacka P, Sundaraj R, Celik I, Yahya EB, Dubey A, Zerroug E, Kontek R. Epigallocatechin-3-gallate therapeutic potential in cancer: mechanism of action and clinical implications. *Molecules* **2023**;*28*:5246.
64. Rashidi B, Malekzadeh M, Goodarzi M, Masoudifar A, Mirzaei H. Green tea and its anti-angiogenesis effects. *Biomed Pharmacother*. **2017**;*89*:949.
65. Rodriguez SK, Guo W, Liu L, Band MA, Paulson EK, Meydani M. Green tea catechin, epigallocatechin-3-gallate, inhibits vascular endothelial growth factor angiogenic signaling by disrupting the formation of a receptor complex. *Int J Cancer* **2006**;*118*:1635.
66. Wang L, Liu WQ, Broussy S, Han B, Fang H. Recent advances of anti-angiogenic inhibitors targeting VEGF/VEGFR axis. *Front Pharmacol*. **2023**;*14*: 1307860.
67. Harris-Tryon TA, Grice EA. Microbiota and maintenance of skin barrier function. *Science* **2022**;*376*:940.
68. Chen YE, Fischbach MA, Belkaid Y. Skin microbiota-host interactions. *Nature* **2018**;*553*:427.
69. Almoughrabie S, Cau L, Cavagnero K, O'Neill AM, Li F, Roso-Mares A, Mainzer C, Closs B, Kolar MJ, Williams KJ, Bensinger SJ, Gallo RL. Commensal *Cutibacterium acnes* induce epidermal lipid synthesis important for skin barrier function. *Sci Adv*. **2023**;*9*: eadg6262.
70. Hou K, Wu ZX, Chen XY, Wang JQ, Zhang D, Xiao C, Zhu D, Koya JB, Wei L, Li J, Chen ZS. Microbiota in health and diseases. *Signal Transduct Target Ther*. **2022**;*7*: 135.
71. Fyhrquist N, Muirhead G, Prast-Nielsen S, et al. Microbe-host interplay in atopic dermatitis and psoriasis. *Nat Commun*. **2019**;*10*:4703.
72. Zhang Q, Shi L, He H, Liu X, Huang Y, Xu D, Yao M, Zhang N, Guo Y, Lu Y, Li H, Zhou J, Tan J, Xing M, Luo G. Down-regulating scar formation by microneedles directly via a mechanical communication pathway. *ACS Nano* **2022**;*16*:10163.
73. Liu L, Yu H, Long Y, You Z, Ogawa R, Du Y, Huang C. Asporin inhibits collagen matrix-mediated intercellular mechanocommunications between fibroblasts during keloid progression. *FASEB J*. **2021**;*35*: e21705.
74. Sedaghat ES, Gold MH. Skin care for scars: where we have been and what's new. *Dermatol Rev*. **2023**;*4*:278.
75. Hoeksema H, De Vos M, Verbelen J, Pirayesh A, Monstrey S. Scar management by means of occlusion and hydration: a comparative study of silicones versus a hydrating gel-cream. *Burns* **2013**;*39*:1437.
76. Nguyen N, Dulai AS, Adnan S, Khan Z-e-h, Sivamani RK. Narrative review of the use of hydrocolloids in dermatology: applications and benefits. *J Clin Med*. **2025**;*14*: 1345.